ACS NANO
Cite This: ACS Nano 2019, 13, 10682−10693
www.acsnano.org

ARTICLE

Analysis of the Limits of the Near-Field Produced by Nanoparticle Arrays

Alejandro Manjavacas,* Lauren Zundel, and Stephen Sanders

Department of Physics and Astronomy, University of New Mexico, Albuquerque, New Mexico 87131, United States

Supporting Information

ABSTRACT: **Periodic arrays are an exceptionally interesting arrangement for metallic nanostructures because of their ability to support collective lattice resonances. These modes, which arise from the coherent multiple scattering enabled by the lattice periodicity, give rise to very strong and spectrally narrow optical responses. Here, we investigate the enhancement of the near-field produced by the lattice resonances of arrays of metallic nanoparticles when illuminated with a plane wave. We find that, for infinite arrays, this enhancement can be made arbitrarily large by appropriately designing the geometrical characteristics of the array. On the other hand, in the case of finite arrays, the near-field enhancement is limited by the number of elements of the array that interact coherently. Furthermore, we show that, as the near-field enhancement increases, the length scale over which it extends above and below the array becomes larger and its spectral linewidth narrows. We also analyze the impact that material losses have on these behaviors. As a direct application of our results, we investigate the interaction between a nanoparticle array and a dielectric slab placed a certain distance above it and show that the extraordinary near-field enhancement produced by the lattice resonance can lead to very strong interactions, even at significantly large separations. This work provides a detailed characterization of the limits of the near-field produced by lattice resonances and, therefore, advances our knowledge of the optical response of periodic arrays of nanostructures, which can be used to design and develop applications exploiting the extraordinary properties of these systems.**

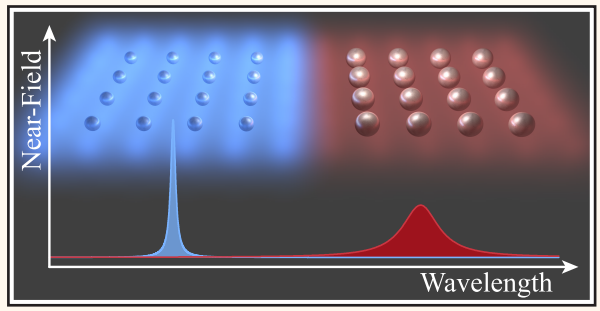

KEYWORDS: *near-field enhancement, periodic arrays, nanoparticle arrays, lattice resonances, plasmons, plasmonic crystals*

Metallic nanostructures possess free electrons that, when illuminated with light of the right frequency, give rise to coherent oscillations known as surface plasmons.[1] These excitations interact strongly with light, confining it into subwavelength volumes, and therefore, producing very large field enhancements,[2,3] which have already been exploited in a variety of applications. These include improved solar energy harvesting,[4,5] photocatalysis,[6,7] ultrasensitive biosensing,[8,9] and nanoscale light emission,[10−12] to cite a few.

In a large number of applications, metallic nanostructures are arranged in periodic arrays,[13−15] which, in addition to contributing to the amplification of the response of the individual constituents, can give rise to collective behaviors associated with the periodicity of the system.[16−20] Lattice resonances are a paradigmatic example of these collective responses.[14−16,21−24] These resonances, which arise from the coherent multiple scattering between the elements of the array, occurring at wavelengths commensurate with the lattice periodicity, display very strong optical responses with narrow spectral linewidths.[25−30] Because of these exceptional properties, systems supporting lattice resonances have been used to design ultrasensitive sensors,[31−33] different types of light emitting devices,[34−45] lenses,[46] color printing approaches,[47−49] and platforms for quantum information processing,[50−54] as well as to enhance nonlinear responses,[55−58] and to investigate interesting physical phenomena.[59−61]

The strong optical response produced by lattice resonances is usually reflected in the far-field behavior of the array, resulting, for instance, in large values of the array reflectance. This quantity, as well as other far-field characteristics of the array, such as the transmittance and the absorbance, are bounded to a range from 0 to 1, so, at most, the excitation of a lattice resonance can enhance them to unity. However, this is not the case for the near-field response of the array. For example, the electric field in its vicinity, which is also increased by the excitation of a lattice resonance,[62−64] is not bounded and, in principle, could be enhanced arbitrarily. Therefore, two questions arise: (i) what is the strongest enhancement of the near-field that a lattice resonance, supported by a periodic array of nanostructures, can produce and (ii) under which conditions can this field enhancement be achieved?

Received: June 26, 2019
Accepted: September 5, 2019
Published: September 5, 2019

DOI: 10.1021/acsnano.9b05031
ACS Nano 2019, 13, 10682−10693

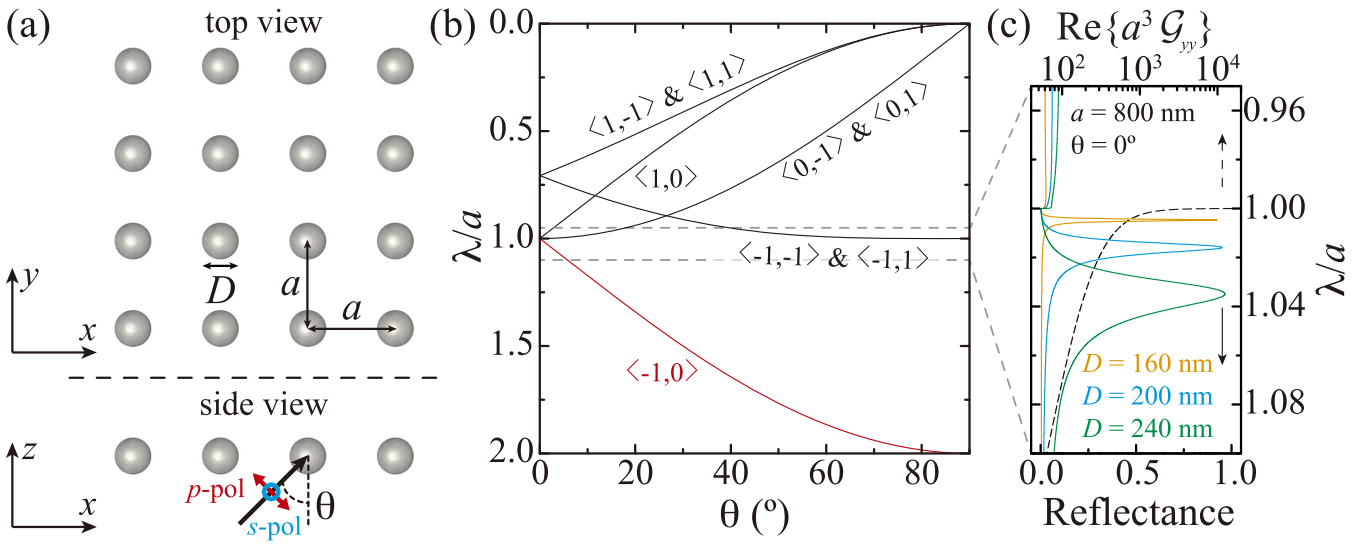

Figure 1. Periodic arrays of metallic nanoparticles. (a) Schematics of the system under study, consisting of a square array of identical silver nanospheres with diameter *D*, separated by a center-to-center distance *a*. The array is located in the *xy* plane, is assumed to be in vacuum, and is excited by a plane wave propagating with wavevector $\mathbf{k} = (2\pi/\lambda)[\sin(\theta)\hat{\mathbf{x}} + \cos(\theta)\hat{\mathbf{z}}]$, as indicated in the lower panel. (b) Dispersion diagram showing the first five Rayleigh anomaly bands for the array. (c) Reflectance for three different arrays with *D* = 160 nm (yellow curve), *D* = 200 nm (blue curve), and *D* = 240 nm (green curve), calculated at normal incidence (*i.e.*, $\theta = 0°$) for $\lambda \approx a$ (lower axis). In all of the cases, *a* = 800 nm. The black dashed curve represents the real part of the in-plane component (*i.e.*, *yy*) of the lattice sum (upper axis).

Here, we seek to answer these questions by performing a detailed analysis of the mechanisms that give rise to the near-field enhancement produced by the lattice resonances of periodic arrays of nanostructures. To that end, we combine an analytical approach with rigorous solutions of Maxwell's equations. We find that, for infinite arrays, the near-field enhancement produced by the excitation of a lattice resonance can be made arbitrarily large. However, for finite arrays, the maximum enhancement is limited by the number of constituents that can interact coherently. Furthermore, we show that, in parallel with the growth of the near-field enhancement, there is an increase in the length scale over which this enhancement extends above and below the array. Our results shed light on the near-field characteristics of the lattice resonances supported by periodic arrays of nanostructures.

RESULTS AND DISCUSSION

The system under study is depicted in Figure 1a. It consists of a square array of identical silver spherical nanoparticles with diameter *D* separated by a center-to-center distance *a*. The array, which is located in the *xy* plane, is assumed to be in vacuum, and is illuminated with a plane wave of amplitude $\mathbf{E}_0$ and wavelength λ, propagating with wavevector $\mathbf{k} = (2\pi/\lambda)[\sin(\theta)\hat{\mathbf{x}} + \cos(\theta)\hat{\mathbf{z}}]$. In all of the calculations, we use tabulated data to describe the dielectric function of silver.[65] When the size of the particles is both much smaller than the wavelength of light and a small fraction of the array period, the optical response of the array can be described using the well-established coupled dipole model (CDM).[16,20,21,27] Within this approach, each nanosphere in the array is modeled as a point electric dipole characterized by a frequency-dependent polarizability α, which can be calculated from the dipolar Mie scattering coefficient.[66] The dipole induced at the particle located at position $\mathbf{R}_l = x_l\hat{\mathbf{x}} + y_l\hat{\mathbf{y}}$ satisfies

$$\mathbf{p}_l = \alpha \mathbf{E}_0 e^{ikx_l \sin\theta} + \alpha \sum_{m \neq l} \mathbf{G}_{lm}\mathbf{p}_m \tag{1}$$

where $\mathbf{G}_{lm} = [k^2\mathcal{I} + \nabla\nabla]e^{ik|\mathbf{R}_l - \mathbf{R}_m|}/|\mathbf{R}_l - \mathbf{R}_m|$ is the dipole–dipole interaction tensor, with $\mathcal{I}$ being the 3 × 3 identity matrix and $k = 2\pi/\lambda$. Thanks to the periodicity of the array, the solutions of eq 1 satisfy Bloch's theorem and, hence, can be written as $\mathbf{p}_l = \mathbf{p}(\theta)e^{ikx_l \sin\theta}$ with

$$\mathbf{p}(\theta) = \mathbf{A}\mathbf{E}_0 \tag{2}$$

Here, $\mathbf{A} = [\alpha^{-1}\mathcal{I} - \mathcal{G}(\theta)]^{-1}$ is the effective polarizability of the array, and

$$\mathcal{G}(\theta) = \sum_{l \neq 0}^{\infty} \mathbf{G}_{l0} e^{-ikx_l \sin\theta} \tag{3}$$

is the Fourier transform of the dipole–dipole interaction tensor, commonly known as the lattice sum.[16] This quantity, which can be efficiently calculated using Ewald's method,[16,67,68] contains the information about the geometry of the array and, therefore, determines its collective behavior.[20] Specifically, the lattice resonances appear at wavelengths corresponding to the poles of the effective polarizability of the array or, in other words, when

$$Re\{\alpha^{-1} - \mathcal{G}_{ss}(\theta)\} \simeq 0 \tag{4}$$

with *s* = *x*, *y*, and *z* for the in-plane and out-of-plane cases, respectively. This happens in the vicinity of the Rayleigh anomaly bands, when a diffracted beam becomes grazing, and therefore $\mathcal{G}(\theta)$ diverges. The wavelength of these spectral features is determined, for our particular configuration, by the condition $\lambda = 2\pi/|k\sin\theta\ \hat{\mathbf{x}} + \mathbf{q}|$, where $\mathbf{q}$ represents the reciprocal lattice vectors of the array.[16,20] The first five Rayleigh anomaly bands for the square array under consideration are shown in Figure 1b as a function of the incidence angle θ. Notice that we use the notation $\langle l, m\rangle$ to

DOI: 10.1021/acsnano.9b05031
ACS Nano 2019, 13, 10682–10693

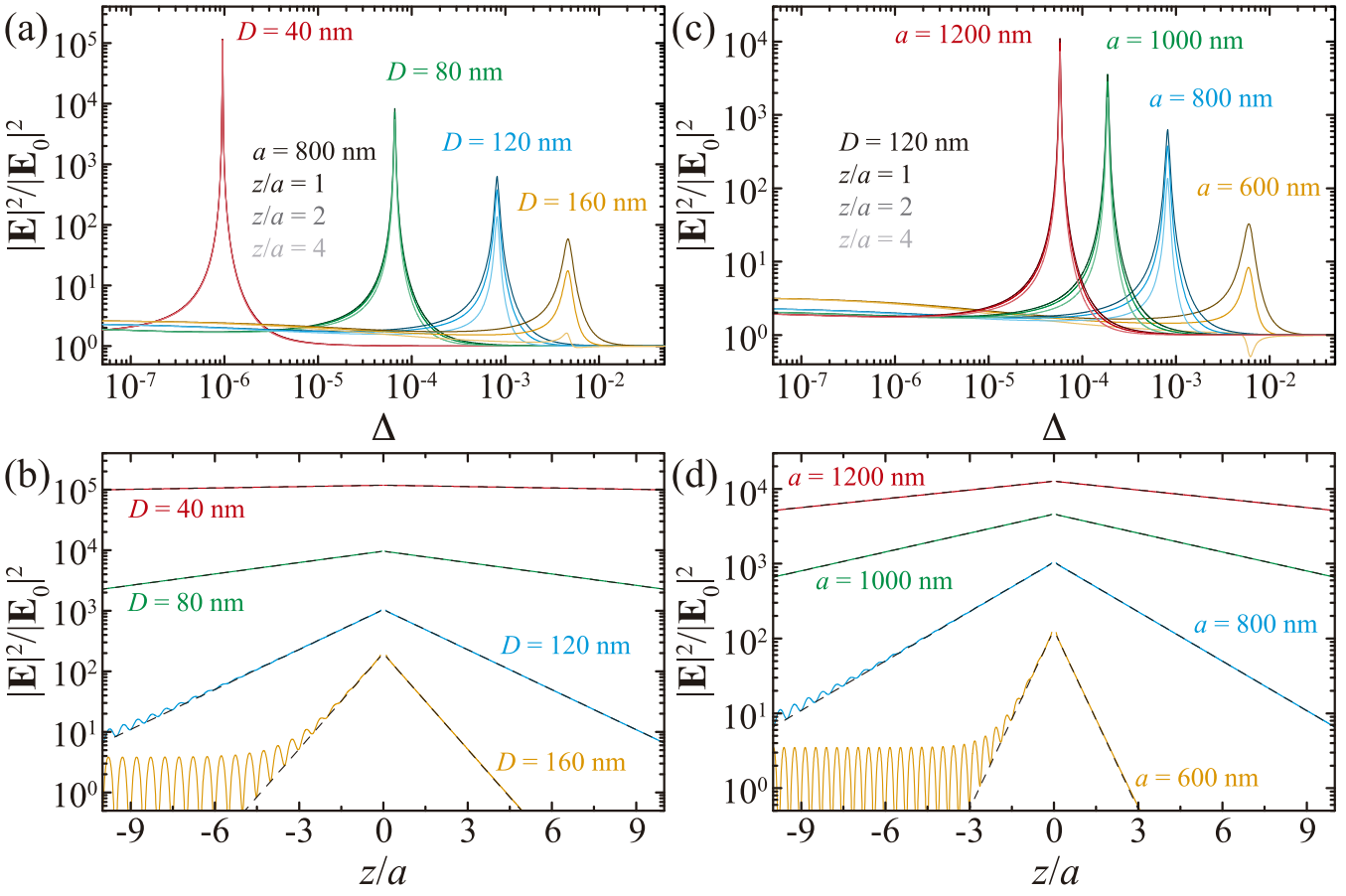

Figure 2. Analysis of the near-field produced by the array. (a) Enhancement of the near-field intensity as a function of the spectral detuning, $\Delta = \lambda/a - 1$, for an array with a = 800 nm and D = 40 nm (red curves), D = 80 nm (green curves), D = 120 nm (blue curves), and D = 160 nm (yellow curves). The enhancement is calculated at three different distances above the array: $z = a$, $z = 2a$, and $z = 4a$, as indicated by the shade of the color of the curve. (b) Spatial dependence of the near-field intensity at resonance for the arrays studied in panel a (solid curves). The black dashed curves represent the approximated results obtained using eq 6. (c, d) Same as in panels a and b, but in this case, the diameter of the nanoparticles is kept at D = 120 nm, while the array period is a = 1200 nm (red curves), a = 1000 nm (green curves), a = 800 nm (blue curves), and a = 600 nm (yellow curves). In all cases, we assume normal incidence (*i.e.*, $\theta = 0°$), and the near-field intensity is averaged over a unit cell.

label the Rayleigh anomaly band corresponding to the reciprocal lattice vector $\mathbf{q} = \frac{2\pi}{a}(l\hat{\mathbf{x}} + m\hat{\mathbf{y}})$.

Figure 1c shows the reflectance spectrum calculated at normal incidence near the first Rayleigh anomaly ($\lambda = a$) for three different arrays, all of them with a = 800 nm, and either D = 240 nm (green curve), D = 200 nm (blue curve), or D = 160 nm (yellow curve). These spectra display a lattice resonance that results in a very high reflectance. As expected from eq 4, the decrease in the diameter of the particle and, therefore, in its polarizability results in a shift of the lattice resonance toward wavelengths closer to the Rayleigh anomaly, for which the lattice sum becomes larger, as shown by the black dashed curve.

The results shown in Figure 1c, as well as in the remainder of this work, are obtained by rigorously solving Maxwell's equations using a multiple elastic scattering of multipolar expansions (MESME) approach.[69−74] However, as stated above, the CDM is accurate for arrays composed of small metallic particles and, therefore, allows us to obtain deeper insight into the physics behind the lattice resonances (see Figure S1 for a comparison of the MESME approach and the CDM). In particular, exploiting this approach, the near-field produced by these excitations at a point $\mathbf{r} = (\mathbf{R}, z)$ can be written as (see Methods)

$$\mathbf{E}(\mathbf{r}) = \frac{2\pi i}{a^2}\sum_{\mathbf{q}}[k^2\mathcal{I} + \nabla\nabla]\mathbf{p}(\theta)e^{ikx\sin\theta}e^{i\mathbf{q}\cdot\mathbf{R}}\frac{e^{ik_{z\mathbf{q}}|z|}}{k_{z\mathbf{q}}} \quad (5)$$

where $k_{z\mathbf{q}} = \sqrt{k^2 - (k\sin\theta\hat{\mathbf{x}} + \mathbf{q})^2}$ and $\mathbf{p}(\theta)$ is given in eq 2. This expression involves a sum over all reciprocal lattice vectors. For a given lattice resonance, each of them results in either an evanescent or a propagating diffracted beam, depending on whether $|k\sin\theta\,\hat{\mathbf{x}} + \mathbf{q}|$ is smaller or larger than k and, thus, if $k_{z\mathbf{q}}$ is a real or pure imaginary number. Only those $\mathbf{q}$ resulting in propagating beams contribute to the far-field response of the array. In contrast, the near-field is determined by both propagating and evanescent diffracted beams. However, the contribution of each evanescent beam strongly depends on the value of the corresponding $k_{z\mathbf{q}}$. This quantity controls how fast the electric field decays with $|z|$, as well as how strong its amplitude is.

It is important to note that every lattice resonance appears in the spectrum next to a Rayleigh anomaly or, in other words, near a wavelength at which $k_{z\mathbf{q}}$ vanishes for a certain $\mathbf{q}$ and, therefore, $\mathcal{G}$ diverges. Then, following eq 5, it appears possible

DOI: 10.1021/acsnano.9b05031
ACS Nano 2019, 13, 10682−10693

to obtain an arbitrarily large near-field that extends to arbitrarily long distances from the array by tuning its properties so that the wavelength of the lattice resonance approaches that of the corresponding Rayleigh anomaly. For instance, let us consider the lattice resonance located on the red side of the first Rayleigh anomaly (see Figure 1b) and assume that the array is illuminated with a field of normal incidence polarized along the y axis. Under these conditions, the resulting enhancement of the near-field intensity near the array, averaged over the unit cell, can be approximated as

$$\frac{|\mathbf{E}|^2}{|\mathbf{E}_0|^2} \approx \left(1 + \frac{4\pi}{3}\xi\right)^{-2} \frac{e^{-|z|/L_z}}{\Delta} \tag{6}$$

Here, $\Delta = \lambda/a - 1$ is the normalized spectral detuning with respect to the first Rayleigh anomaly, which is located at $\lambda = a$ for $\theta = 0°$, $\xi = \sigma_{abs}/\sigma_{sca}$ is the ratio between the dipolar absorption, $\sigma_{abs} = 4\pi k(Im\{\alpha\} - 2k^3|\alpha|^2/3)$, and scattering, $\sigma_{sca} = 8\pi k^4|\alpha|^2/3$, cross sections of the nanoparticle at the resonance wavelength, and $L_z = a/(4\pi\sqrt{2\Delta})$ is the decay length along the z axis. This expression for the enhancement is obtained from eq 5 by taking into account only the terms corresponding to $\mathbf{q} = \pm (2\pi/a)\hat{\mathbf{x}}$, which are the reciprocal lattice vectors associated with the $\langle \pm 1,0\rangle$ Rayleigh anomalies, and performing the average over the entire unit cell (see Methods for a detailed derivation). From examination of eq 6, it is clear that, as Δ decreases, the near-field intensity grows, due to the $1/\Delta$ factor, and extends over a larger region, thanks to the increase in L_z. According to eq 4, this exceptional behavior can be achieved by making the response of the individual nanostructures weaker, either by decreasing their diameter or reducing their area density (*i.e.*, increasing the array period).

To confirm these predictions, we calculate the enhancement of the near-field intensity above the array from the rigorous solution of Maxwell's equations using the MESME approach. We perform these calculations for arrays with a = 800 nm and different values of D, assuming normal incidence. In all cases, we consider three different values of z and average the results over the unit cell (see Figure S2 for the spatial distribution of the near-field). The outcome of these calculations is plotted in Figure 2a as a function of Δ (see Figure S3 for plots as a function of wavelength). As predicted by the CDM, the enhancement of the near-field intensity grows as the diameter of the particles becomes smaller and, consequently, the value of Δ for the lattice resonance decreases. In particular, for $z = a$, it increases from values around 10^2 for D = 160 nm (yellow curves), to values around 10^3 and 10^4 for D = 120 nm (blue curves) and D = 80 nm (green curves), respectively, or even larger when D is further reduced. We want to stress that these values correspond to the near-field intensity averaged over the entire unit cell, rather than a peak value at a hot spot. As this happens, the linewidth of the resonance becomes smaller, resulting in very large quality factors, Q, as we discuss later. Furthermore, comparing the results obtained for $z = a$, $z = 2a$, and $z = 4a$, we observe that the enhancement extends to larger distances away from the array as the particle diameter decreases. This effect is analyzed in more detail in panel b, where we investigate the dependence of the near-field intensity with z. In this case, we consider both positive and negative values of z, corresponding, respectively, to positions above and below the array. As expected, when the value of Δ for the lattice resonance decreases, L_z becomes larger, and, consequently, the near-field intensity decays more slowly. This spatial dependence is well predicted by the CDM, whose results, obtained using eq 6 with the value of Δ taken from panel a, are shown by the black dashed curves. The CDM predictions are in perfect agreement with the full numerical calculations when the enhancement of the field intensity is much larger than one, thus proving that the origin of this enhancement is the evanescent field produced by the diffracted beam associated with the reciprocal lattice vectors $\mathbf{q} = \pm\frac{2\pi}{a}\hat{\mathbf{x}}$. The agreement worsens when this contribution decreases and its interference with the incident and the specularly reflected fields, which are not considered in eq 6, becomes significant and produces the oscillations appearing at negative z for the two arrays with the largest diameters. We want to note that, despite the field extending multiple wavelengths away from the array, we choose to refer to it throughout the manuscript as near-field because of its evanescent character.

An alternative path to shift the lattice resonance closer to the Rayleigh anomaly, without changing the size of the particle, is to increase the period of the array. This results in a decrease of the lattice sum, $\mathcal{G}$, and therefore, in light of eq 4, the value of Δ for the lattice resonance. We explore this possibility in Figure 2c, where we perform similar calculations to those shown in panel a, but in this case, we keep the diameter of the particles fixed to D = 120 nm and change the period of the array, as indicated by the legend. Analyzing these results, we verify that, as a increases, the lattice resonance moves to smaller Δ and the maximum enhancement of the near-field intensity grows, reaching very large values. Furthermore, this enhancement extends farther away, as can be seen by comparing the results for $z = a$ with those obtained at $z = 2a$ and $z = 4a$. This is further confirmed by the full spatial dependence analyzed in panel d, which, as in the previous case, is in very good quantitative agreement with the results of the CDM (black dashed curves).

An interesting prediction of eq 6 is that the material losses in the nanoparticles affect the near-field intensity enhancement through the factor $\left(1 + \frac{4\pi}{3}\xi\right)^{-2}$. Specifically, lower material losses should result in smaller values of ξ, and therefore larger enhancements. However, this behavior is expected to saturate once $4\pi\xi/3 \ll 1$, and further decrease in the material losses should not impact the maximum achievable enhancement. A similar behavior is expected for the quality factor of the resonance. Indeed, as shown in the Methods section, the full width at half-maximum of the lattice resonance can be approximated, within the CDM, by $\Gamma \approx \left(1 + \frac{4\pi}{3}\xi\right)(2\Delta)^{3/2}$, which leads to $Q \approx \left(1 + \frac{4\pi}{3}\xi\right)^{-1}(2\Delta)^{-3/2}$ for $\Delta \ll 1$. This expression also explains the increase in Q as Δ approaches zero observed in the results plotted in Figure 2, which is consistent with previous works.[16,75−78] It is also important to note that, since the energy associated with the near-field of the lattice resonance is proportional to $|\mathbf{E}|^2 L_z$, which scales as $\Delta^{-3/2}$, the scaling of Γ as $\Delta^{3/2}$ ensures the energy stored in the system upon excitation with a light pulse of finite duration will always be finite.

To verify these predictions of the CDM, we perform full numerical calculations of the near-field enhancement at the lattice resonance wavelength, for arrays with a = 800 nm and different diameters. In all cases, the enhancements are calculated at a distance $z = a$ above the arrays and the results

DOI: 10.1021/acsnano.9b05031
ACS Nano 2019, 13, 10682−10693

averaged over the entire unit cell. We perform these calculations assuming different levels of material losses, which we obtain by multiplying the imaginary part of the tabulated dielectric function of silver[65] by a factor γ, leaving the real part unchanged. This approach is equivalent to modifying the damping coefficient of a Drude model (to which the tabulated data can be fitted) and, therefore, preserves Kramers–Kronig relations in the limit of the damping being much smaller than the frequencies of interest. Examining the results of these calculations, which are plotted in Figure 3a

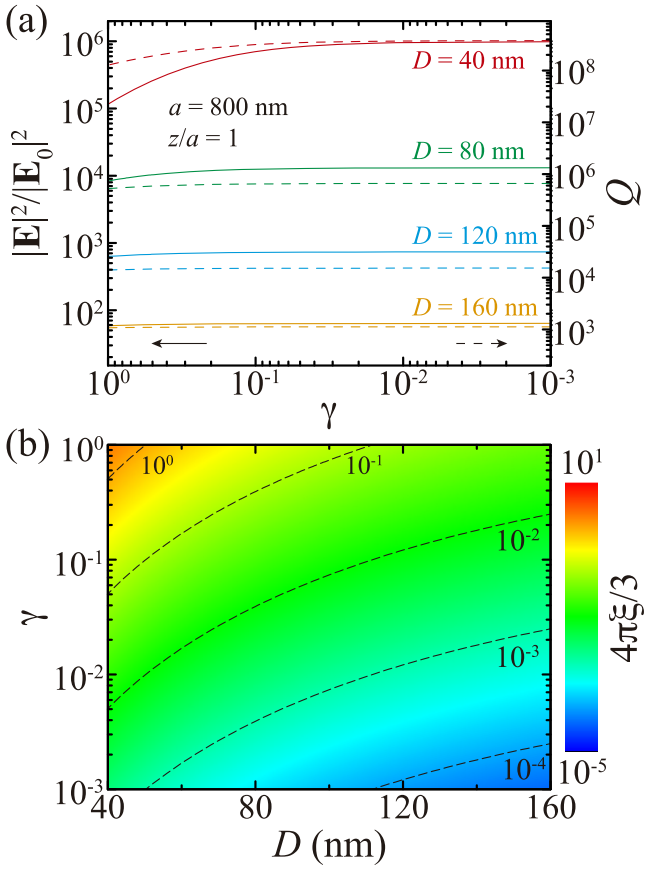

Figure 3. Effect of material losses. (a) Maximum enhancement of the field intensity (left axis) and quality factor (right axis) for the lattice resonance calculated, as a function of the material losses, for arrays with a = 800 nm and different diameters. In these calculations, the imaginary part of the dielectric function of the nanoparticles is multiplied by a factor γ, as explained in the text. In all cases, we assume normal incidence (*i.e.*, $\theta = 0°$), and the field intensity is calculated at $z = a$ and averaged over a unit cell. (b) Contour plot of the factor $4\pi\xi/3$, defined after eq 6, as a function of D and γ, calculated for a wavelength λ = 800 nm. The dashed curves signal the contours corresponding to the values indicated by the labels.

with solid curves (left axis), we observe that, as expected, the decrease in the material losses results in a larger near-field intensity enhancement that eventually saturates. A similar saturation behavior is observed for the quality factor (dashed curves, right axis). This quantity is calculated as the ratio between the spectral position of the near-field intensity enhancement peak and its full width at half-maximum,[79] both of which are obtained from a Lorentzian fitting of the numerical data. It is worth noting that these results are perfectly reproduced by the expression for Q given above.

Interestingly, the level of losses for which the saturation occurs varies with the particle diameter, shifting to smaller values of γ as D decreases. We explain this behavior by noting that, for a fixed wavelength, ξ scales approximately as D^{-3}, since $\sigma_{abs} \propto D^3$ and $\sigma_{sca} \propto D^6$. This is confirmed by Figure 3b, where we plot the value of $4\pi\xi/3$ as a function of D and γ for a wavelength $\lambda = a$. Clearly, for a fixed value of γ, this factor decreases with D, which confirms that the impact of losses on the field intensity enhancement and the quality factor becomes more important as the particle size decreases. This analysis is also useful to extrapolate our predictions to arrays made of individual constituents without material losses, such as dielectric nanostructures[80] and atoms.[52−54]

So far, we have analyzed the response of the arrays to normal incidence illumination, but a similar field enhancement is expected to occur when light is incident at other angles.[14,15] Oblique illumination allows the spectral position of the lattice resonance to be shifted without altering the geometry of the array because the position of the Rayleigh anomalies is dependent on the angle of incidence. As a result of this dependence, the degeneracy between the $\langle \pm 1,0 \rangle$ Rayleigh anomalies is broken for $\theta \neq 0°$, and the $\langle -1,0 \rangle$ anomaly becomes the one appearing at the lowest energy, with a wavelength given by $a(1 + \sin\theta)$, as shown in Figure 1b. Furthermore, oblique incidence also breaks the degeneracy between *s*- and *p*-polarized illumination.

Figure 4a shows the enhancement of the field intensity above an array with D = 120 nm and a = 800 nm calculated for *s*-polarized illumination using the MESME approach. The enhancement is calculated for different values of z above the array and averaged over the unit cell. We consider seven different angles of incidence ranging from 1° to 80°, as indicated by the legend. As θ increases, the lattice resonance moves toward smaller values of Δ, which, for $\theta \neq 0°$, is given by $\Delta = \lambda/(a + a \sin\theta) - 1$ (notice that this definition of Δ reduces to the one previously given for normal incidence). This initially produces the expected increase in the near-field intensity enhancement, however, for $\theta > 20°$, the enhancement becomes smaller despite the decrease in Δ, leaving an optimum angle of incidence. We can explain this behavior using the insight provided by the CDM. Specifically, we attribute the decrease in the near-field enhancement to the combination of two effects happening as θ increases: (i) the resonance wavelength increases, thus resulting in smaller values of k that reduce the coupling to the external illumination, and (ii) the imaginary part of the effective polarizability of the array becomes smaller, thus reducing the value of the induced dipole. However, this is not the case for the decay length, which, for oblique incidence, is given by $L_z = a\sqrt{1 + \sin\theta}/(4\pi\sqrt{2\Delta})$ (see Methods), and therefore grows as θ increases and, consequently, Δ decreases. This is clearly shown by the solid curves in panel c, which display the spatial dependence of the field intensity enhancement above and below the array for θ = 1°, 20°, and 80°. As the angle of incidence increases, the curves become flatter, denoting a larger value of L_z, a behavior that has been observed previously.[25,78]

The other configuration we investigate corresponds to the array being illuminated with *p*-polarized light. In this case, the incident light excites a dipole in the nanoparticles that oscillates out of plane,[81] along the z axis, which results in a different coupling mediated by $\mathcal{G}_{zz}(\theta)$ instead of $\mathcal{G}_{yy}(\theta)$.

DOI: 10.1021/acsnano.9b05031
ACS Nano 2019, 13, 10682−10693

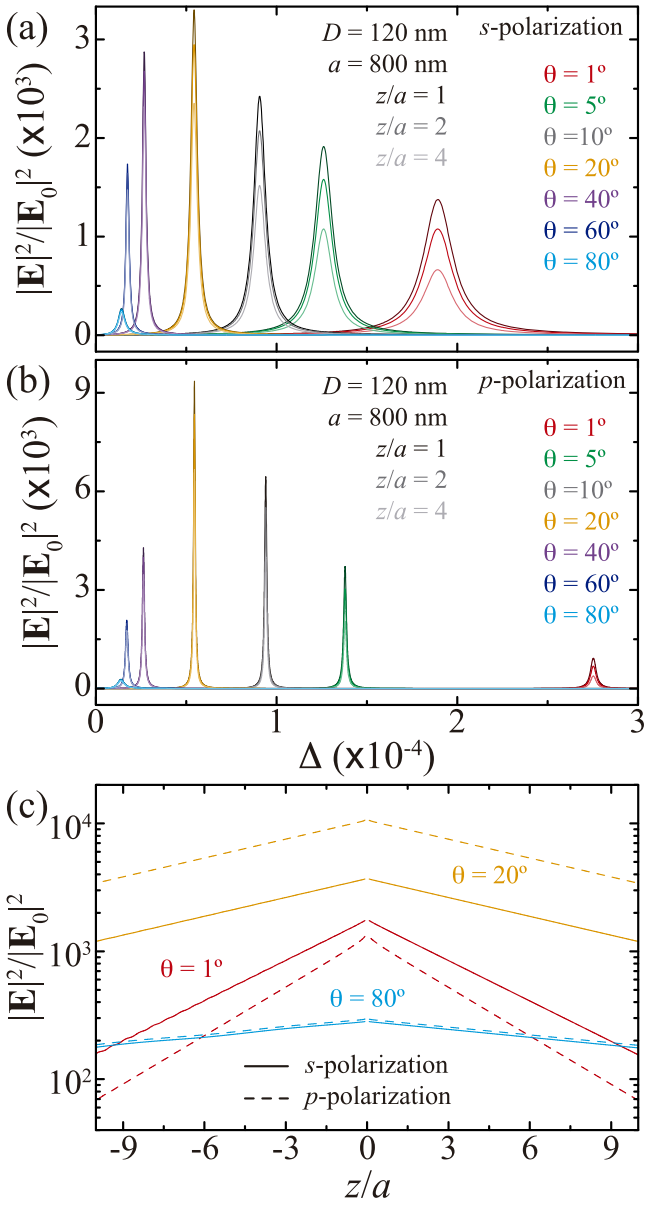

Figure 4. Angle dependence of the near-field produced by the array. (a) Enhancement of the field intensity as a function of the spectral detuning, $\Delta = \lambda/(a + a \sin\theta) - 1$, for an array with a = 800 nm and D = 120 nm, which is illuminated with an *s*-polarized plane wave at different incidence angles θ, as indicated by the legend. The enhancement of the field intensity is calculated at three different distances above the array, $z = a$, $z = 2a$, and $z = 4a$, as indicated by the shade of the color. (b) Same as in panel a but for *p*-polarized illumination. (c) Spatial dependence of the field intensity at resonance for some of the arrays studied in panels a (solid curves) and b (dashed curves). In all cases, the field intensity is averaged over a unit cell.

Nonetheless, the decay length is given by $L_z = a\sqrt{1 + \sin\theta}/(4\pi\sqrt{2\Delta})$, as was the case for *s*-polarization. The corresponding results for the near-field intensity enhancement are shown in Figure 4b, for the same array investigated in panel a and for the same angles of incidence. Similar to the case of *s*-polarized illumination, we find that the field enhancement reaches a maximum at $\theta \approx 20°$. This behavior can be traced back, again, to the shift in the lattice resonance wavelength and the decrease in the imaginary part of the effective polarizability caused by the change in θ, which counters the enhancement provided by the decrease in Δ. Despite these similarities, the resonances for *p*-polarization are significantly narrower than their counterparts for *s*-polarized illumination, following what has been observed in the past when analyzing the angular dependence of the far-field properties of similar arrays.[78,82] Furthermore, the field intensity enhancements tend to be larger for the *p*-polarized case, except for $\theta = 1°$, for which the lattice resonance is located at a significantly larger Δ than in the corresponding *s*-polarized case. These larger enhancements can also be seen in panel c by comparing the dashed and solid curves. Doing so also confirms that the decay lengths for *p*- and *s*-polarized illumination are almost identical when the value of Δ for the corresponding resonances is similar and increase with θ,[25,78] as expected from the definition of L_z.

The origin of the predicted large field enhancement associated with the lattice resonance of an array of nanostructures, as well as its spatial extent, can be traced back to the perfectly periodic nature of the system, which requires it to contain an infinite number of elements. As we have discussed above, the near-field increases and extends farther away from the array as the wavelength of the lattice resonance moves closer to that of the corresponding Rayleigh anomaly. This can be achieved by weakening the response of each of the nanostructures, either by decreasing their size or reducing the number of them per unit area (*i.e.*, increasing the array period). Although this leads to smaller individual contributions to the field enhancement, the phase of each of these contributions becomes increasingly uniform, thus resulting in a stronger collective response. Interestingly, this effect could explain recent observations of the increase in the nonlinear response of arrays of metallic nanoparticles as their density is reduced.[83]

That said, obtaining an arbitrarily large field enhancement is only possible because the array contains an infinite number of elements, and therefore, the real part of the lattice sum, $\mathcal{G}$, becomes infinite at the Rayleigh anomaly (indeed, it diverges as $1/\sqrt{\Delta}$, as shown in ref 84, see also Figure S4), thus making it possible to satisfy Equation 4 for any particle size or lattice period.[16] However, in reality, any fabricated array is finite, which imposes an upper limit on the value of the lattice sum, and therefore, on the field enhancement. Finite-size effects on the far-field response of arrays have been analyzed in the past using different approaches.[85−88] In our case, we can again use the CDM to estimate the impact that the finite size of the array has on the field enhancement. Specifically, we can analyze a truncated version of the lattice sum defined in eq 3, in which, instead of summing over an infinite number of array elements, we restrict it to a subset of $(N + 1) \times (N + 1)$ particles. Physically, this truncated lattice sum represents the field at the position of the central particle of a $(N + 1) \times (N + 1)$ array produced by all of the other elements. By comparing the real parts of the truncated lattice sum and α^{-1}, we can thus estimate a lower bound on the number of elements necessary to achieve the near-field enhancements predicted in this work.

Figure 5 displays the real part of the truncated lattice sum as a function of Δ for different values of N, as indicated in the legend. We consider normal incidence and hence focus on the *yy* component, which is the only relevant one for these illumination conditions (see Figure S5 for other angles of incidence and the *zz* component). As anticipated, the truncated lattice sum tends to a finite value as Δ approaches

DOI: 10.1021/acsnano.9b05031
ACS Nano 2019, 13, 10682−10693

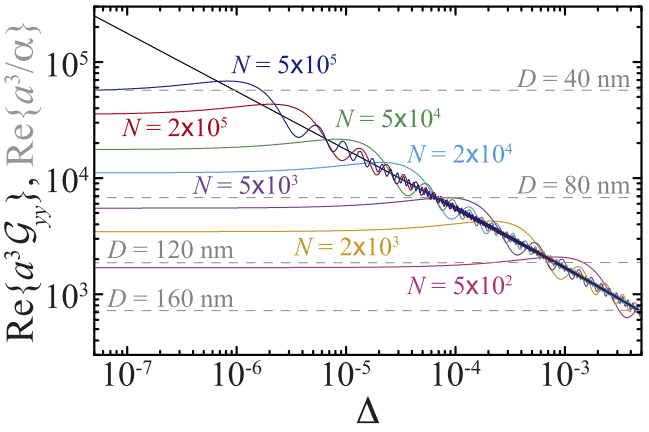

Figure 5. Finite-size effects on the lattice sum. Real part of the in-plane component (*i.e.*, *yy*) of the lattice sum calculated for normal incidence (*i.e.*, $\theta = 0°$), as a function of the spectral detuning, Δ (black curve). The color curves represent the results obtained by truncating the lattice sum for an array of size $(N + 1) \times (N + 1)$, as described in the text. The gray dashed lines indicate the real part of the inverse of the nanoparticle polarizability calculated for different values of *D*. In all cases, we assume $a = 800$ nm.

zero, in sharp contrast with the divergent behavior of the lattice sum for an infinite array, which is shown by the black curve. As N increases, this finite value grows and the truncated lattice sum converges to that of the infinite array, oscillating around it over a range that extends to increasingly smaller values of Δ. This makes it possible to intersect the real part of α^{-1}, which is plotted with gray dashed curves, for the same value of Δ as the infinite array, and thus fulfill eq 4. Therefore, for a given value of D, we can use the results of Figure 5 to obtain an approximate estimation of the minimum number of elements that an array needs to contain to produce the near-field enhancements discussed in the previous sections. We want to emphasize that this analysis applies to the predictions of the collective response of any periodic array of structures, regardless of the particular nature of their individual constituents.[52−54,80] It is also worth noting that, in a practical realization, the fabrication imperfections, which cause deviations in the size and positioning of nanostructures, will further raise the necessary number of elements in the array, since these inhomogeneities will effectively decrease the number of particles that are coherently interacting.[88−90]

The large values of the near-field enhancement provided by these arrays, as well as the broad region over which they extend away from the arrays, can be exploited for many interesting applications, in which the near-field produced by the array interacts with other photonic elements, like atoms, molecules, or quantum dots. To explore that possibility, we investigate how the presence of a dielectric slab modifies the reflectance of the array. Specifically, we consider a slab of thickness $t = 100$ nm, made of a material with dielectric function $\varepsilon_s = 1 + \delta\varepsilon$, and located a distance d above the array, as depicted in Figure 6a. We compute the change in the reflectance of the array, $R - R_0$, with respect to the value obtained in absence of the slab, always assuming normal incidence. Panel b shows the results for an array of nanospheres with $D = 160$ nm and period $a = 800$ nm. We consider two different dielectric functions: $\delta\varepsilon = 10^{-3}(1 + i)$ (solid curves) and $\delta\varepsilon = 10^{-4}(1 + i)$ (dashed curves), as well as two different distances: $d = a$ (red curves) and $d = 4a$ (blue curves). Examining these results, we observe

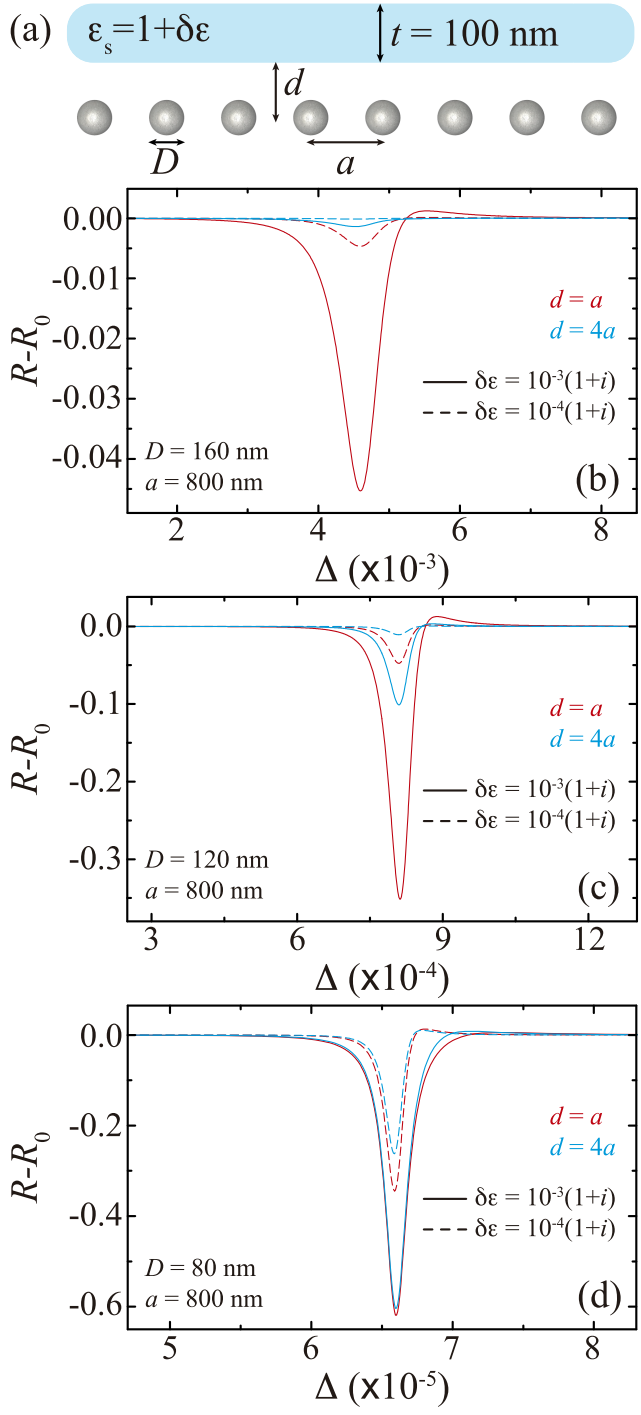

Figure 6. Interaction between the array and other photonic structures. (a) Schematics of the system under study. (b) Change in the reflectance of an array with $a = 800$ nm and $D = 160$ nm when a slab of thickness $t = 100$ nm and dielectric function $\varepsilon_s = 1 + \delta\varepsilon$ is placed a distance d above the array, as shown in the schematics. We consider four different combinations of d and $\delta\varepsilon$, as indicated in the legend. (c, d) Same as in panel b but for arrays with $D = 120$ nm and $D = 80$ nm, respectively. In all cases, we assume normal incidence (*i.e.*, $\theta = 0°$).

that, for $d = a$ and $\delta\varepsilon = 10^{-3}(1 + i)$, there is a change in the reflectance of around 0.04. As expected, this value decreases when either the slab is moved to $d = 4a$ or its dielectric function is reduced to $\delta\varepsilon = 10^{-4}(1 + i)$ and becomes almost zero for the case with $d = 4a$ and $\delta\varepsilon = 10^{-4}(1 + i)$.

DOI: 10.1021/acsnano.9b05031
ACS Nano 2019, 13, 10682−10693

The change in the reflectance becomes more pronounced when the size of the particles in the array is reduced, since this, as we have shown before, leads to an increase in the near-field enhancement as well as the decay length. This effect can be seen in panels c and d, which display the results for arrays with D = 120 nm and D = 80 nm, respectively. In particular, we observe that, in these two cases, it is possible to resolve the presence of a slab with $\delta\varepsilon = 10^{-4}(1 + i)$ situated at a distance $d = 4a$. Indeed, for D = 80 nm, the large decay length results in changes of reflectance that are almost identical for $d = a$ and $d = 4a$. All of these results highlight the potential of periodic arrays of nanoparticles to generate large near-fields that can lead to strong interactions with other photonic elements placed at distances up to several wavelengths from the arrays. Importantly, such strong interaction also makes these systems very sensitive to asymmetries or losses in the dielectric environment,[73] as discussed in Figure S7.

CONCLUSIONS

In summary, we have provided a comprehensive analysis of the limits of the near-field produced by the lattice resonances supported by periodic arrays of nanoparticles. By combining an analytical approach, based on the coupled dipole model, with rigorous solutions of Maxwell's equations, we have shown that, for infinite arrays, the near-field enhancement produced by the lattice resonances can be made arbitrarily large. This is accompanied by a narrowing of the linewidth of the resonance and a growth of the near-field decay length in the direction perpendicular to the array, therefore, leading to exceptionally large fields that extend over significantly broad regions around the array. We have derived an analytical expression for the near-field enhancement and used it to show that such behaviors are obtained by reducing the size of the particles or their density in the array, both of which result in a shift of the spectral position of the lattice resonance closer to the corresponding Rayleigh anomaly, as well as to study the role of material losses in the array response. Furthermore, we have analyzed the extent to which this extraordinary effect, which is a direct consequence of the infinite nature of the array, holds for realistic systems with finite size, finding that both the value of the near-field and its spatial extent are limited by the number of particles in the array that interact coherently. Finally, as an application of these results, we have studied the interaction of these arrays with a dielectric slab placed parallel to them and shown that the large near-field, as well as the long decay length, can lead to very strong couplings, even at distances of a few wavelengths. These results show that periodic arrays of nanostructures can provide near-field enhancements comparable to, or even larger than, those produced by individual plasmonic systems with sharp features or small gaps, but over extended volumes with dimensions much larger than the wavelength. Therefore, these systems can be an ideal platform for applications exploiting the contributions from near-field modes, such as energy and heat transfer. For these reasons, our work provides a valuable understanding of the near-field produced by the lattice resonances of periodic arrays of nanostructures, and therefore will serve to guide experimental efforts seeking to exploit the extraordinary optical response of these systems.

METHODS

Derivation of Equations 5 and 6. Working within the CDM approach,[16,20,21,27] we start by writing the explicit form of the near-field produced, at a position $\mathbf{r} = (\mathbf{R}, z)$, by an array of dipoles

$$\mathbf{E}(\mathbf{r}) = \sum_l [k^2 \mathcal{I} + \nabla\nabla]\frac{e^{ik|\mathbf{r}-\mathbf{R}_l|}}{|\mathbf{r}-\mathbf{R}_l|}\mathbf{p}_l$$

where $k = 2\pi/\lambda$, with λ being the wavelength of light, $\mathbf{p}_l$ is the dipole induced in the particle located at $\mathbf{R}_l$, and $\mathcal{I}$ is the 3 × 3 identity matrix. Then, using the Weyl identity,[79] this expression can be rewritten as

$$\mathbf{E}(\mathbf{r}) = \sum_l [k^2 \mathcal{I} + \nabla\nabla]\frac{i}{2\pi}\int \frac{d\mathbf{k}'_\parallel}{k'_z} e^{i\mathbf{k}'_\parallel\cdot(\mathbf{R}-\mathbf{R}_l)} e^{ik'_z|z|}\mathbf{p}_l \tag{7}$$

with $k'_z = \sqrt{k^2 - (\mathbf{k}'_\parallel)^2}$. Assuming that the array is illuminated with a plane wave of amplitude $\mathbf{E}_0$, which propagates with wavevector $\mathbf{k} = (2\pi/\lambda)[\sin(\theta)\hat{\mathbf{x}} + \cos(\theta)\hat{\mathbf{z}}]$, the induced dipole can be written as $\mathbf{p}_l = \mathbf{p}(\theta)e^{ikx_l \sin\theta}$. Furthermore, thanks to the periodicity of the array, we have that[16]

$$\sum_l e^{i(k\sin\theta\hat{\mathbf{x}} - \mathbf{k}_\parallel)\cdot\mathbf{R}_l} = \frac{4\pi^2}{a^2}\sum_{\mathbf{q}} \delta(\mathbf{k}'_\parallel - k\sin\theta\hat{\mathbf{x}} - \mathbf{q})$$

where $\mathbf{q}$ are the reciprocal lattice vectors of the array and a is its period. Then, using these expressions and Bloch's theorem into eq 7, we can readily obtain eq 5, which we reproduce here in an extended version

$$\begin{bmatrix} E_x(\mathbf{r}) \\ E_y(\mathbf{r}) \\ E_z(\mathbf{r}) \end{bmatrix} = \frac{2\pi i}{a^2}\sum_{\mathbf{q}} \begin{bmatrix} 1 - \frac{(k\sin\theta + q_x)^2}{k^2} & \frac{-(k\sin\theta + q_x)q_y}{k^2} & \mp\frac{(k\sin\theta + q_x)k_{z\mathbf{q}}}{k^2} \\ \frac{-q_y(k\sin\theta + q_x)}{k^2} & 1 - \frac{q_y^2}{k^2} & \mp\frac{q_y k_{z\mathbf{q}}}{k^2} \\ \mp\frac{(k\sin\theta + q_x)k_{z\mathbf{q}}}{k^2} & \mp\frac{q_y k_{z\mathbf{q}}}{k^2} & 1 - \frac{k_{z\mathbf{q}}^2}{k^2} \end{bmatrix} \begin{bmatrix} p_x(\theta) \\ p_y(\theta) \\ p_z(\theta) \end{bmatrix} k^2 e^{ikx\sin\theta} e^{i\mathbf{q}\cdot\mathbf{R}} \frac{e^{ik_{z\mathbf{q}}|z|}}{k_{z\mathbf{q}}} \tag{8}$$

where $k_{z\mathbf{q}} = \sqrt{k^2 - (k\sin\theta\hat{\mathbf{x}} + \mathbf{q})^2}$ and the upper (lower) signs apply for $z > 0$ ($z < 0$).

In the case of illumination at normal incidence (*i.e.*, $\theta = 0°$) with $\mathbf{E}_0 = E_0\hat{\mathbf{y}}$, only the y-component of the dipole is excited, and therefore, eq 8 reduces to

$$\begin{bmatrix} E_x(\mathbf{r}) \\ E_y(\mathbf{r}) \\ E_z(\mathbf{r}) \end{bmatrix} = \frac{2\pi i}{a^2}\sum_{\mathbf{q}} \begin{bmatrix} -q_x q_y \\ k^2 - q_y^2 \\ \mp q_y k_{z\mathbf{q}} \end{bmatrix} p_y(0) e^{i\mathbf{q}\cdot\mathbf{R}} \frac{e^{ik_{z\mathbf{q}}|z|}}{k_{z\mathbf{q}}}$$

As explained in the Article, for wavelengths close enough to a given Rayleigh anomaly, this sum is dominated by the term associated with the corresponding reciprocal lattice vector due to the vanishing of $k_{z\mathbf{q}}$.

DOI: 10.1021/acsnano.9b05031
ACS Nano 2019, 13, 10682−10693

Therefore, working close to the first Rayleigh anomaly and using eq 2, the near-field produced by the array can be approximated as

$$\frac{E_y(\mathbf{r})}{E_0} \approx \frac{4\pi i}{a^2} k^2 [\alpha^{-1} - \mathcal{G}_{yy}(0)]^{-1} \cos\left(\frac{2\pi}{a}x\right) \frac{e^{i\sqrt{k^2-(2\pi/a)^2}\,|z|}}{\sqrt{k^2-(2\pi/a)^2}} \tag{9}$$

where the cosine function appears because, at normal incidence, both $\mathbf{q} = (2\pi/a)\hat{\mathbf{x}}$ and $\mathbf{q} = -(2\pi/a)\hat{\mathbf{x}}$ contribute equally to the field because of the degeneration of $k_{z\mathbf{q}}$. We can further simplify this equation by noting that, at resonance

$$[\alpha^{-1} - \mathcal{G}_{yy}(0)]^{-1} \simeq \frac{1}{iIm\{\alpha^{-1} - \mathcal{G}_{yy}(0)\}}$$

where $Im\{\alpha^{-1}\} = -Im\{\alpha\}/|\alpha|^2$ can be written in terms of the dipolar absorption, $\sigma_{abs} = 4\pi k(Im\{\alpha\} - 2k^3|\alpha|^2/3)$, and scattering, $\sigma_{sca} = 8\pi k^4|\alpha|^2/3$, cross sections of the nanoparticles as

$$Im\{\alpha^{-1}\} = -2k^3(1+\xi)/3 \tag{10}$$

with $\xi = \sigma_{abs}/\sigma_{sca}$. Furthermore, again using the Weyl identity,[79] the lattice sum can be written as[20]

$$\mathcal{G}_{yy}(0) = \frac{2\pi i}{a^2}\sum_{\mathbf{q}} \frac{k^2 - q_y^2}{k_{z\mathbf{q}}} - \frac{i}{2}\int_0^\infty dQ \frac{2k^2Q - Q^3}{\sqrt{k^2-Q^2}}$$

and, therefore, its imaginary part, for wavelengths $\lambda > a$, reduces to

$$Im\{\mathcal{G}_{yy}(0)\} = \frac{2\pi k}{a^2} - \frac{2k^3}{3} \tag{11}$$

Then, using all of these expressions, we can rewrite eq 9 as

$$\frac{E_y(\mathbf{r})}{E_0} \approx 2i\cos\left(\frac{2\pi}{a}x\right)\left[1 + \frac{4\pi}{3}\xi\right]^{-1} \frac{e^{-|z|/(2L_z)}}{\sqrt{2\Delta}}$$

where we have introduced the spectral detuning $\Delta = \lambda/a - 1$ and the decay length $L_z = a/(4\pi\sqrt{2\Delta})$. Taking the square of this expression and averaging over the unit cell, we obtain eq 6. Furthermore, this expression predicts a $\cos^2(2\pi x/a)$ dependence for the near-field intensity enhancement produced by the array, which agrees perfectly with the results obtained from the full numerical calculation using the MESME approach[69−74] that are shown in the first two rows of Figure S2.

When the array is illuminated at oblique incidence, the degeneracy between the $\mathbf{q} = (2\pi/a)\hat{\mathbf{x}}$ and $\mathbf{q} = -(2\pi/a)\hat{\mathbf{x}}$ is lifted. In such a case, next to the $\langle -1,0\rangle$ Rayleigh anomaly appearing at $\lambda = a(1 + \sin\theta)$, the electric field is dominated by the term associated with $\mathbf{q} = -(2\pi/a)\hat{\mathbf{x}}$. Therefore, from eq 8 and the definition of $k_{z\mathbf{q}}$, the expressions for the spectral detuning, Δ, and the decay length, L_z, for non-normal illumination become $\Delta = \lambda/(a + a\sin\theta) - 1$ and $L_z = a\sqrt{1+\sin\theta}/(4\pi\sqrt{2\Delta})$, respectively. Furthermore, the aforementioned breakdown of the degeneracy also implies that, for oblique incidence, the field intensity within the unit cell becomes uniform and does not depend on the in-plane coordinates x and y. This prediction is in excellent agreement with the results of the MESME approach plotted in the two lower rows of Figure S2.

Lattice Resonance Linewidth. The linewidth of the field enhancement produced by the lattice resonance decreases as it moves closer to the Rayleigh anomaly (see, for instance, Figure 2). We can explain this behavior by exploiting the insight provided by the CDM. Specifically, we know that, for normal incidence, the spectral characteristics of the enhancement produced by a lattice resonance are mainly determined by the expression $|\alpha^{-1} - \mathcal{G}_{yy}(0)|^{-2}$. We can calculate the full width at half-maximum of the lattice resonance, Γ, by assuming that $|\alpha^{-1} - \mathcal{G}_{yy}(0)|^{-2}$ has a Lorentzian profile. Then, performing a Taylor expansion of this expression around the lattice resonance condition, we get

$$|\alpha^{-1} - \mathcal{G}_{yy}(0)|^{-2} \approx \left[\left(\frac{\Gamma}{2}\frac{\partial}{\partial\Delta}Re\{\mathcal{G}_{yy}(0)\}\right)^2 + (Im\{\alpha^{-1} - \mathcal{G}_{yy}(0)\})^2\right]^{-1}$$

To obtain this expression, we have used the fact that, at resonance $Re\{\alpha^{-1} - \mathcal{G}_{yy}(0)\} \simeq 0$, as well as $\partial Re\{\alpha^{-1}\}/\partial\Delta \ll \partial Re\{\mathcal{G}_{yy}(0)\}/\partial\Delta$, and $(\Gamma/2)\partial Im\{\alpha^{-1} - \mathcal{G}_{yy}(0)\}/\partial\Delta \ll Im\{\alpha^{-1} - \mathcal{G}_{yy}(0)\}$. These approximations are justified by the almost constant behavior of $Re\{\alpha^{-1}\}$ and $Im\{\alpha^{-1} - \mathcal{G}_{yy}(0)\}$ in the spectral range of interest, as can be seen in Figure S4. Therefore, we can write

$$\Gamma \approx \frac{2Im\{\alpha^{-1} - \mathcal{G}_{yy}(0)\}}{\frac{\partial}{\partial\Delta}Re\{\mathcal{G}_{yy}(0)\}}$$

Then, noting that, as shown in refs 84 and 16, for a square lattice of period a, $Re\{a^3\mathcal{G}_{yy}(0)\} \approx 4\sqrt{2}\pi^2\Delta^{-1/2} - 118$ (see also Figure S4), and using eqs 10 and 11, we finally get

$$\Gamma \approx \left(1 + \frac{4\pi}{3}\xi\right)(2\Delta)^{3/2}$$

Notice that Γ is unitless, since it represents the full width at half-maximum of the lattice resonance when expressed in terms of Δ. The corresponding quality factor of the resonance, Q, can be then approximated, for $\Delta \ll 1$, as

$$Q = \frac{\Delta + 1}{\Gamma} \approx \left(1 + \frac{4\pi}{3}\xi\right)^{-1}(2\Delta)^{-3/2}$$

ASSOCIATED CONTENT

Supporting Information

The Supporting Information is available free of charge on the ACS Publications website at DOI: 10.1021/acsnano.9b05031.

Comparison of the coupled dipole model (CDM) with rigorous solutions of Maxwell's equations, obtained using both a multiple-scattering of multipolar expansions (MESME) approach and a finite element method (FEM) approach; analysis of the in-plane spatial dependence of the field intensity enhancement produced by the arrays; plot of the near-field intensity enhancement as a function of wavelength; analysis of the mechanisms determining the linewidth of the lattice resonances; analysis of the truncated lattice sum, similar to that in Figure 5, but for different angles of incidence and polarizations; and analysis of the effect of homogeneous and asymmetric dielectric environments (PDF)

AUTHOR INFORMATION

Corresponding Author

*E-mail: manjavacas@unm.edu.

ORCID

Alejandro Manjavacas: 0000-0002-2379-1242

Notes

The authors declare no competing financial interest.

ACKNOWLEDGMENTS

This work has been sponsored by the U.S. National Science Foundation (Grant ECCS-1710697). We would like to thank the UNM Center for Advanced Research Computing, supported in part by the U.S. National Science Foundation, for providing the computational resources used in this work.

DOI: 10.1021/acsnano.9b05031
ACS Nano 2019, 13, 10682−10693

L.Z. acknowledges support from the Rayburn Reaching Up Fund and the New Mexico Space Grant Consortium. We are also grateful to Prof. Javier García de Abajo for valuable and enjoyable discussions.

REFERENCES

(1) Maier, S. A. *Plasmonics: Fundamentals and Applications*; Springer: New York, 2007.
(2) Álvarez-Puebla, R. A.; Liz-Marzán, L. M.; García de Abajo, F. J. Light Concentration at the Nanometer Scale. *J. Phys. Chem. Lett.* **2010**, *1*, 2428−2434.
(3) Halas, N. J.; Lal, S.; Chang, W.; Link, S.; Nordlander, P. Plasmons in Strongly Coupled Metallic Nanostructures. *Chem. Rev.* **2011**, *111*, 3913−3961.
(4) Catchpole, K. R.; Polman, A. Plasmonic Solar Cells. *Opt. Express* **2008**, *16*, 21793−21800.
(5) Atwater, H. A.; Polman, A. Plasmonics for Improved Photovoltaic Devices. *Nat. Mater.* **2010**, *9*, 205−213.
(6) Baffou, G.; Quidant, R. Nanoplasmonics for Chemistry. *Chem. Soc. Rev.* **2014**, *43*, 3898−3907.
(7) Brongersma, M. L.; Halas, N. J.; Nordlander, P. Plasmon-Induced Hot Carrier Science and Technology. *Nat. Nanotechnol.* **2015**, *10*, 25−34.
(8) Xu, H.; Bjerneld, E. J.; Käll, M.; Börjesson, L. Spectroscopy of Single Hemoglobin Molecules by Surface Enhanced Raman Scattering. *Phys. Rev. Lett.* **1999**, *83*, 4357−4360.
(9) Anker, J. N.; Hall, W. P.; Lyandres, O.; Shah, N. C.; Zhao, J.; Van Duyne, R. P. Biosensing with Plasmonic Nanosensors. *Nat. Mater.* **2008**, *7*, 442−453.
(10) Lu, Y.-J.; Kim, J.; Chen, H.-Y.; Wu, C.; Dabidian, N.; Sanders, C. E.; Wang, C.-Y.; Lu, M.-Y.; Li, B.-H.; Qiu, X.; Chang, W.-H.; Chen, L.-J.; Shvets, G.; Shih, C.-K.; Gwo, S. Plasmonic Nanolaser Using Epitaxially Grown Silver Film. *Science* **2012**, *337*, 450−453.
(11) Yang, A.; Odom, T. W. Breakthroughs in Photonics 2014: Advances in Plasmonic Nanolasers. *IEEE Photonics J.* **2015**, *7* (7), 1−6.
(12) Liu, K.; Li, N.; Sadana, D. K.; Sorger, V. J. Integrated Nanocavity Plasmon Light Sources for On-Chip Optical Interconnects. *ACS Photonics* **2016**, *3*, 233−242.
(13) Ross, M. B.; Mirkin, C. A.; Schatz, G. C. Optical Properties of One-, Two-, and Three Dimensional Arrays of Plasmonic Nanostructures. *J. Phys. Chem. C* **2016**, *120*, 816−830.
(14) Wang, W.; Ramezani, M.; Väkeväinen, A. I.; Törmä, P.; Gómez Rivas, J.; Odom, T. W. The Rich Photonic World of Plasmonic Nanoparticle Arrays. *Mater. Today* **2018**, *21*, 303−314.
(15) Kravets, V. G.; Kabashin, A. V.; Barnes, W. L.; Grigorenko, A. N. Plasmonic Surface Lattice Resonances: A Review of Properties and Applications. *Chem. Rev.* **2018**, *118*, 5912−5951.
(16) García de Abajo, F. J. Colloquium: Light Scattering by Particle and Hole Arrays. *Rev. Mod. Phys.* **2007**, *79*, 1267−1290.
(17) Fructos, A. L.; Campione, S.; Capolino, F.; Mesa, F. Characterization of Complex Plasmonic Modes in Two-Dimensional Periodic Arrays of Metal Nanospheres. *J. Opt. Soc. Am. B* **2011**, *28*, 1446−1458.
(18) Humphrey, A. D.; Barnes, W. L. Plasmonic Surface Lattice Resonances on Arrays of Different Lattice Symmetry. *Phys. Rev. B: Condens. Matter Mater. Phys.* **2014**, *90*, No. 075404.
(19) Guo, R.; Hakala, T. K.; Törmä, P. Geometry Dependence of Surface Lattice Resonances in Plasmonic Nanoparticle Arrays. *Phys. Rev. B: Condens. Matter Mater. Phys.* **2017**, *95*, 155423.
(20) Baur, S.; Sanders, S.; Manjavacas, A. Hybridization of Lattice Resonances. *ACS Nano* **2018**, *12*, 1618−1629.
(21) Zhao, L.; Kelly, K. L.; Schatz, G. C. The Extinction Spectra of Silver Nanoparticle Arrays: Influence of Array Structure on Plasmon Resonance Wavelength and Width. *J. Phys. Chem. B* **2003**, *107*, 7343−7350.
(22) Auguié, B.; Barnes, W. L. Collective Resonances in Gold Nanoparticle Arrays. *Phys. Rev. Lett.* **2008**, *101*, 143902.
(23) Kravets, V. G.; Schedin, F.; Grigorenko, A. N. Extremely Narrow Plasmon Resonances BasedonDiffractionCouplingofLocalizedPlasmonsinArraysofMetallicNanoparticles. *Phys. Rev. Lett.* **2008**, *101*, No. 087403.
(24) Chu, Y.; Schonbrun, E.; Yang, T.; Crozier, K. B. Experimental Observation of Narrow Surface Plasmon Resonances in Gold Nanoparticle Arrays. *Appl. Phys. Lett.* **2008**, *93*, 181108.
(25) Vecchi, G.; Giannini, V.; Gómez Rivas, J. Surface Modes in Plasmonic Crystals Induced by Diffractive Coupling of Nanoantennas. *Phys. Rev. B: Condens. Matter Mater. Phys.* **2009**, *80*, No. 201401(R).
(26) Giannini, V.; Vecchi, G.; Gómez Rivas, J. Lighting Up Multipolar Surface Plasmon Polaritons by Collective Resonances in Arrays of Nanoantennas. *Phys. Rev. Lett.* **2010**, *105*, 266801.
(27) Teperik, T. V.; Degiron, A. Design Strategies to Tailor the Narrow Plasmon-Photonic Resonances in Arrays of Metallic Nanoparticles. *Phys. Rev. B: Condens. Matter Mater. Phys.* **2012**, *86*, 245425.
(28) Almpanis, E.; Papanikolaou, N.; Auguié, B.; Tserkezis, C.; Stefanou, N. Diffractive Chains of Plasmonic Nanolenses: Combining Near-Field Focusing and Collective Enhancement Mechanisms. *Opt. Lett.* **2012**, *37*, 4624−4626.
(29) Yang, A.; Hryn, A. J.; Bourgeois, M. R.; Lee, W.-K.; Hu, J.; Schatz, G. C.; Odom, T. W. Programmable and Reversible Plasmon Mode Engineering. *Proc. Natl. Acad. Sci. U. S. A.* **2016**, *113*, 14201−14206.
(30) Le-Van, Q.; Zoethout, E.; Geluk, E.-J.; Ramezani, M.; Berghuis, M.; Gómez Rivas, J. Enhanced Quality Factors of Surface Lattice Resonances in Plasmonic Arrays of Nanoparticles. *Adv. Opt. Mater.* **2019**, *7*, 1801451.
(31) Adato, R.; Yanik, A. A.; Amsden, J. J.; Kaplan, D. L.; Omenetto, F. G.; Hong, M. K.; Erramilli, S.; Altug, H. Ultra-Sensitive Vibrational Spectroscopy of Protein Monolayers with Plasmonic Nanoantenna Arrays. *Proc. Natl. Acad. Sci. U. S. A.* **2009**, *106*, 19227−19232.
(32) Thackray, B. D.; Kravets, V. G.; Schedin, F.; Auton, G.; Thomas, P. A.; Grigorenko, A. N. Narrow Collective Plasmon Resonances in Nanostructure Arrays Observed at Normal Light Incidence for Simplified Sensing in Asymmetric Air and Water Environments. *ACS Photonics* **2014**, *1*, 1116−1126.
(33) Danilov, A.; Tselikov, G.; Wu, F.; Kravets, V. G.; Ozerov, I.; Bedu, F.; Grigorenko, A. N.; Kabashin, A. V. Ultra-Narrow Surface Lattice Resonances in Plasmonic Metamaterial Arrays for Biosensing Applications. *Biosens. Bioelectron.* **2018**, *104*, 102−112.
(34) Rodriguez, S. R. K.; Lozano, G.; Verschuuren, M. A.; Gomes, R.; Lambert, K.; De Geyter, B.; Hassinen, A.; Van Thourhout, D.; Hens, Z.; Gómez Rivas, J. Quantum Rod Emission Coupled to Plasmonic Lattice Resonances: A Collective Directional Source of Polarized Light. *Appl. Phys. Lett.* **2012**, *100*, 111103.
(35) Lozano, G.; Louwers, D. J.; Rodríguez, S. R. K.; Murai, S.; Jansen, O. T. A.; Verschuuren, M. A.; Gómez Rivas, J. Plasmonics for Solid-State Lighting: Enhanced Excitation and Directional Emission of Highly Efficient Light Sources. *Light: Sci. Appl.* **2013**, *2*, e66.
(36) Zhou, W.; Dridi, M.; Suh, J. Y.; Kim, C. H.; Co, D. T.; Wasielewski, M. R.; Schatz, G. C.; Odom, T. W. Lasing Action In Strongly Coupled Plasmonic Nanocavity Arrays. *Nat. Nanotechnol.* **2013**, *8*, 506−511.
(37) Lozano, G.; Grzela, G.; Verschuuren, M. A.; Ramezani, M.; Rivas, J. G. TailorMade Directional Emission in Nanoimprinted Plasmonic-Based Light-Emitting Devices. *Nanoscale* **2014**, *6*, 9223−9229.
(38) Schokker, A. H.; Koenderink, A. F. Lasing at the Band Edges of Plasmonic Lattices. *Phys. Rev. B: Condens. Matter Mater. Phys.* **2014**, *90*, 155452.
(39) Teperik, T. V.; Degiron, A. Control of Plasmonic Crystal Light Emission. *J. Opt. Soc. Am. B* **2014**, *31*, 223−228.
(40) Ramezani, M.; Lozano, G.; Verschuuren, M. A.; Gómez-Rivas, J. Modified Emission of Extended Light Emitting Layers by Selective Coupling to Collective Lattice Resonances. *Phys. Rev. B: Condens. Matter Mater. Phys.* **2016**, *94*, 125406.
(41) Zakharko, Y.; Held, M.; Graf, A.; Rödlmeier, T.; Eckstein, R.; Hernandez-Sosa, G.; Hähnlein, B.; Pezoldt, J.; Zaumseil, J. Surface

DOI: 10.1021/acsnano.9b05031
ACS Nano 2019, 13, 10682−10693

Lattice Resonances for Enhanced and Directional Electroluminescence at High Current Densities. *ACS Photonics* **2016**, *3*, 2225−2230.
(42) Cotrufo, M.; Osorio, C. I.; Koenderink, A. F. Spin-Dependent Emission from Arrays of Planar Chiral Nanoantennas Due to Lattice and Localized Plasmon Resonances. *ACS Nano* **2016**, *10*, 3389−3397.
(43) Hakala, T. K.; Rekola, H. T.; Väkeväinen, A. I.; Martikainen, J.-P.; Nečada, M.; Moilanen, A. J.; Törmä, P. Lasing in Dark and Bright Modes of a Finite-Sized Plasmonic Lattice. *Nat. Commun.* **2017**, *8*, 13687.
(44) Wang, D.; Yang, A.; Wang, W.; Hua, Y.; Schaller, R. D.; Schatz, G. C.; Odom, T. W. Band-Edge Engineering for Controlled Multi-Modal Nanolasing in Plasmonic Superlattices. *Nat. Nanotechnol.* **2017**, *12*, 889.
(45) Guo, R.; Nečada, M.; Hakala, T. K.; Väkeväinen, A. I.; Törmä, P. Lasing at K Points of a Honeycomb Plasmonic Lattice. *Phys. Rev. Lett.* **2019**, *122*, No. 013901.
(46) Hu, J.; Wang, D.; Bhowmik, D.; Liu, T.; Deng, S.; Knudson, M. P.; Ao, X.; Odom, T. W. Lattice-Resonance Metalenses for Fully Reconfigurable Imaging. *ACS Nano* **2019**, *13*, 4613−4620.
(47) Olson, J.; Manjavacas, A.; Basu, T.; Huang, D.; Schlather, A. E.; Zheng, B.; Halas, N. J.; Nordlander, P.; Link, S. High Chromaticity Aluminum Plasmonic Pixels for Active Liquid Crystal Displays. *ACS Nano* **2016**, *10*, 1108−1117.
(48) Kristensen, A.; Yang, J. K. W.; Bozhevolnyi, S. I.; Link, S.; Nordlander, P.; Halas, N. J.; Mortensen, N. A. Plasmonic Colour Generation. *Nat. Rev. Mater.* **2017**, *2*, 16088.
(49) Esposito, M.; Todisco, F.; Bakhti, S.; Passaseo, A.; Tarantini, I.; Cuscunà, M.; Destouches, N.; Tasco, V. Symmetry Breaking in Oligomer Surface Plasmon Lattice Resonances. *Nano Lett.* **2019**, *19*, 1922−1930.
(50) Väkeväinen, A. I.; Moerland, R. J.; Rekola, H. T.; Eskelinen, A.-P.; Martikainen, J.-P.; Kim, D.-H.; Törmä, P. Plasmonic Surface Lattice Resonances at the Strong Coupling Regime. *Nano Lett.* **2014**, *14*, 1721−1727.
(51) Todisco, F.; Esposito, M.; Panaro, S.; De Giorgi, M.; Dominici, L.; Ballarini, D.; Fernández-Domínguez, A. I.; Tasco, V.; Cuscunà, M.; Passaseo, A.; Ciracì, C.; Gigli, G.; Sanvitto, D. Toward Cavity Quantum Electrodynamics with Hybrid Photon GapPlasmon States. *ACS Nano* **2016**, *10*, 11360−11368.
(52) Bettles, R. J.; Gardiner, S. A.; Adams, C. S. Enhanced Optical Cross Section via Collective Coupling of Atomic Dipoles in a 2D Array. *Phys. Rev. Lett.* **2016**, *116*, 103602.
(53) Shahmoon, E.; Wild, D. S.; Lukin, M. D.; Yelin, S. F. Cooperative Resonances in Light Scattering from Two-Dimensional Atomic Arrays. *Phys. Rev. Lett.* **2017**, *118*, 113601.
(54) Perczel, J.; Borregaard, J.; Chang, D. E.; Pichler, H.; Yelin, S. F.; Zoller, P.; Lukin, M. D. Photonic Band Structure of Two-Dimensional Atomic Lattices. *Phys. Rev. A: At., Mol., Opt. Phys.* **2017**, *96*, No. 063801.
(55) Czaplicki, R.; Kiviniemi, A.; Laukkanen, J.; Lehtolahti, J.; Kuittinen, M.; Kauranen, M. Surface Lattice Resonances in Second-Harmonic Generation from Metasurfaces. *Opt. Lett.* **2016**, *41*, 2684−2687.
(56) Michaeli, L.; Keren-Zur, S.; Avayu, O.; Suchowski, H.; Ellenbogen, T. Nonlinear Surface Lattice Resonance in Plasmonic Nanoparticle Arrays. *Phys. Rev. Lett.* **2017**, *118*, 243904.
(57) Huttunen, M. J.; Rasekh, P.; Boyd, R. W.; Dolgaleva, K. Using Surface Lattice Resonances to Engineer Nonlinear Optical Processes in Metal Nanoparticle Arrays. *Phys. Rev. A: At., Mol., Opt. Phys.* **2018**, *97*, No. 053817.
(58) Hooper, D. C.; Kuppe, C.; Wang, D.; Wang, W.; Guan, J.; Odom, T. W.; Valev, V. K. Second Harmonic Spectroscopy of Surface Lattice Resonances. *Nano Lett.* **2019**, *19*, 165−172.
(59) Rodriguez, S. R. K.; Feist, J.; Verschuuren, M. A.; Garcia Vidal, F. J.; Gómez Rivas, J. Thermalization and Cooling of Plasmon-Exciton Polaritons: Towards Quantum Condensation. *Phys. Rev. Lett.* **2013**, *111*, 166802.
(60) Hakala, T. K.; Moilanen, A. J.; Väkeväinen, A. I.; Guo, R.; Martikainen, J.-P.; Daskalakis, K. S.; Rekola, H. T.; Julku, A.; Törmä, P. Bose−Einstein Condensation in a Plasmonic Lattice. *Nat. Phys.* **2018**, *14*, 739−744.
(61) Abujetas, D. R.; van Hoof, N.; ter Huurne, S.; Gómez Rivas, J. G.; Sánchez-Gil, J. A. Spectral andTemporalEvidenceofRobustPhotonicBoundStatesintheContinuumonTerahertz Metasurfaces. *Optica* **2019**, *6*, 996−1001.
(62) Zou, S.; Schatz, G. C. Silver Nanoparticle Array Structures that Produce Giant Enhancements in Electromagnetic Fields. *Chem. Phys. Lett.* **2005**, *403*, 62−67.
(63) Nikitin, A. G.; Kabashin, A. V.; Dallaporta, H. Plasmonic Resonances in Diffractive Arrays of Gold Nanoantennas: Near and Far Field Effects. *Opt. Express* **2012**, *20*, 27941−27952.
(64) Huang, Y.; Ma, L.; Hou, M.; Zhang, Z. Universal Near-Field Interference Patterns of Fano Resonances in Two-Dimensional Plasmonic Crystals. *Plasmonics* **2016**, *11*, 1377−1383.
(65) Johnson, P. B.; Christy, R. W. Optical Constants of the Noble Metals. *Phys. Rev. B* **1972**, *6*, 4370−4379.
(66) García de Abajo, F. J. Multiple Scattering of Radiation in Clusters of Dielectrics. *Phys. Rev. B: Condens. Matter Mater. Phys.* **1999**, *60*, 6086−6102.
(67) Kambe, K. Theory of Low-Energy Electron Diffraction 2. Cellular Method for Complex Monolayers and Multilayers. *Z. Naturforsch., A: Phys. Sci.* **1968**, *23*, 1280−1294.
(68) Glasser, M. L.; Zucker, I. J. *Theoretical Chemistry: Advances and Perspectives*; New York, 1980; pp 67−139.
(69) Stefanou, N.; Yannopapas, V.; Modinos, A. Heterostructures of Photonic Crystals: Frequency Bands and Transmission Coefficients. *Comput. Phys. Commun.* **1998**, *113*, 49−77.
(70) Stefanou, N.; Yannopapas, V.; Modinos, A. MULTEM 2: A New Version of the Program for Transmission and Band-Structure Calculations of Photonic Crystals. *Comput. Phys. Commun.* **2000**, *132*, 189−196.
(71) García de Abajo, F. J. Interaction of Radiation and Fast Electrons with Clusters of Dielectrics: A Multiple Scattering Approach. *Phys. Rev. Lett.* **1999**, *82*, 2776−2779.
(72) Bendaña, X. M.; García de Abajo, F. J. Confined Collective Excitations of Self-Standing and Supported Planar Periodic Particle Arrays. *Opt. Express* **2009**, *17*, 18826−18835.
(73) Auguié, B.; Bendaña, X. M.; Barnes, W. L.; García de Abajo, F. J. Diffractive Arrays of Gold Nanoparticles Near an Interface: Critical Role of the Substrate. *Phys. Rev. B: Condens. Matter Mater. Phys.* **2010**, *82*, 109039.
(74) Bendaña, X. M.; Lozano, G.; Pirruccio, G.; Gómez Rivas, G.; García de Abajo, F. J. Excitation of Confined Modes on Particle Arrays. *Opt. Express* **2013**, *21*, 5636−5642.
(75) Zou, S.; Schatz, G. C. Narrow Plasmonic/Photonic Extinction and Scattering Line Shapes for One and Two Dimensional Silver Nanoparticle Arrays. *J. Chem. Phys.* **2004**, *121*, 12606−12612.
(76) Zou, S.; Janel, N.; Schatz, G. C. Silver Nanoparticle Array Structures that Produce Remarkably Narrow Plasmon Lineshapes. *J. Chem. Phys.* **2004**, *120*, 10871−10875.
(77) Hicks, E. M.; Zou, S.; Schatz, G. C.; Spears, K. G.; Van Duyne, R. P.; Gunnarsson, L.; Rindzevicius, T.; Kasemo, B.; Käll, M. Controlling Plasmon Line Shapes Through Diffractive Coupling in Linear Arrays of Cylindrical Nanoparticles Fabricated by Electron Beam Lithography. *Nano Lett.* **2005**, *5*, 1065−1070.
(78) Zhou, W.; Hua, Y.; Huntington, M. D.; Odom, T. W. Delocalized Lattice Plasmon Resonances Show Dispersive Quality Factors. *J. Phys. Chem. Lett.* **2012**, *3*, 1381−1385.
(79) Novotny, L.; Hecht, B. *Principles of Nano-Optics*; Cambridge University Press: New York, 2006.
(80) Wang, X.; Kogos, L. C.; Paiella, R. Giant Distributed Optical-Field Enhancements from Mie-Resonant Lattice Surface Modes in Dielectric Metasurfaces. *OSA Continuum* **2019**, *2*, 32−42.
(81) Huttunen, M. J.; Dolgaleva, K.; Törmä, P.; Boyd, R. W. Ultra-Strong Polarization Dependence of Surface Lattice Resonances with Out-of-Plane Plasmon Oscillations. *Opt. Express* **2016**, *24*, 28279−28289.

DOI: 10.1021/acsnano.9b05031
ACS Nano 2019, 13, 10682−10693

(82) Zhou, W.; Odom, T. W. Tunable Subradiant Lattice Plasmons by Out-of-Plane Dipolar Interactions. *Nat. Nanotechnol.* **2011**, *6*, 423.
(83) Czaplicki, R.; Kiviniemi, A.; Huttunen, M. J.; Zang, X.; Stolt, T.; Vartiainen, I.; Butet, J.; Kuittinen, M.; Martin, O. J. F.; Kauranen, M. Less is More: Enhancement of Second-Harmonic Generation from Metasurfaces by Reduced Nanoparticle Density. *Nano Lett.* **2018**, *18*, 7709−7714.
(84) García de Abajo, F. J.; Gómez-Medina, R.; Sáenz, J. J. Full Transmission Through Perfect-Conductor Subwavelength Hole Arrays. *Phys. Rev. E* **2005**, *72*, No. 016608.
(85) Rodriguez, S. R. K.; Schaafsma, M. C.; Berrier, A.; Gómez-Rivas, J. Collective Resonances in Plasmonic Crystals: Size Matters. *Phys. B* **2012**, *407*, 4081−4085.
(86) Matsushima, A. Effect of Periodicity in the Light Scattering from Infinite and Finite Arrays of Silver Nanospheres. *Proc. of 2017 IEEE International Conference on Computational Electromagnetics (ICCEM)* **2017**, 236−237.
(87) Martikainen, J.-P.; Moilanen, A. J.; Törmä, P. Coupled Dipole Approximation Across the Γ-Point in a Finite-Sized Nanoparticle Array. *Philos. Trans. R. Soc., A* **2017**, *375*, 20160316.
(88) Zundel, L.; Manjavacas, A. Finite-Size Effects on Periodic Arrays of Nanostructures. *J. Phys.: Photonics* **2019**, *1*, No. 015004.
(89) Auguié, B.; Barnes, W. L. Diffractive Coupling in Gold Nanoparticle Arrays and the Effect of Disorder. *Opt. Lett.* **2009**, *34*, 401−403.
(90) Schokker, A. H.; Koenderink, A. F. Statistics of Randomized Plasmonic Lattice Lasers. *ACS Photonics* **2015**, *2*, 1289−1297.

DOI: 10.1021/acsnano.9b05031
ACS Nano 2019, 13, 10682−10693

Supporting information for:

Analysis of the Limits of the Near-Field Produced by Nanoparticle Arrays

Alejandro Manjavacas,* Lauren Zundel, and Stephen Sanders

Department of Physics and Astronomy, University of New Mexico, Albuquerque, New Mexico 87131, United States

E-mail: manjavacas@unm.edu

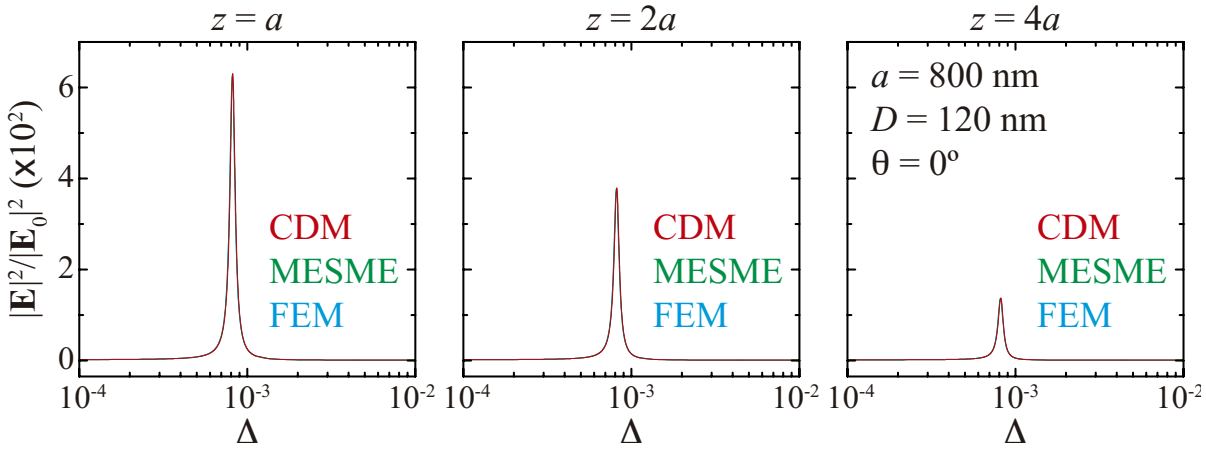

Figure S1: Comparison of the coupled dipole model (CDM) approach (red curves) with rigorous solutions of Maxwell's equations obtained using both a multiple elastic scattering of multipolar expansions (MESME) approach (green curves) and a finite element method (FEM) approach (blue curves). The plots show the enhancement of the field intensity, averaged over the unit cell, and calculated at different distances z above the array. In all cases, we consider an array of silver nanospheres with diameter $D = 120\,\text{nm}$ and period $a = 800\,\text{nm}$, illuminated at normal incidence.

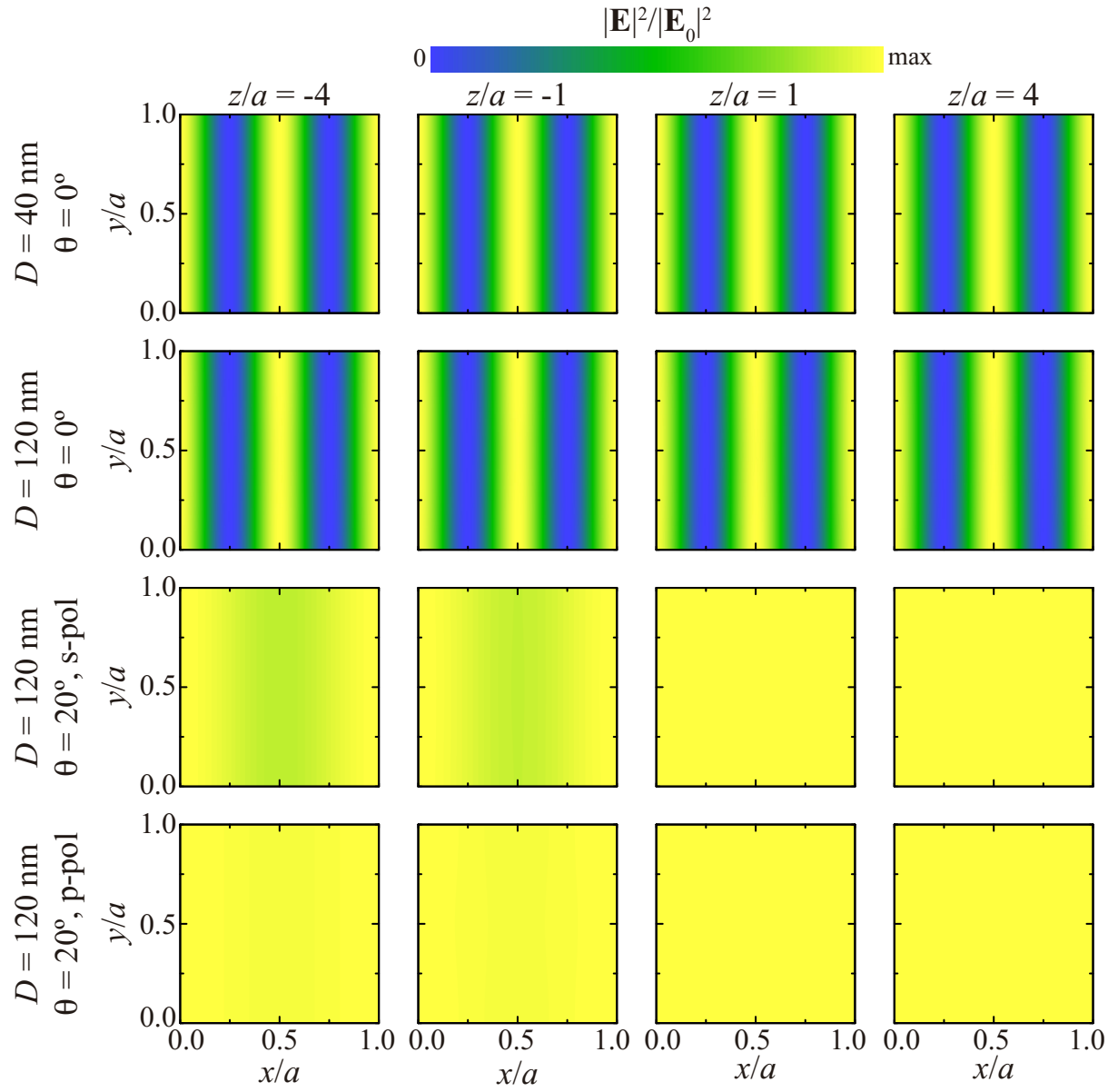

Figure S2: In-plane spatial dependence of the near-field intensity enhancement produced by different arrays. As indicated in the labels, we consider arrays composed of nanospheres of different diameters D, illuminated with light propagating at different angles θ and polarizations, and calculate the field intensity enhancement at different distances above and below the array. In all cases, the period of the array is $a = 800\,\text{nm}$, and the results are normalized to the maximum value of the field intensity enhancement.

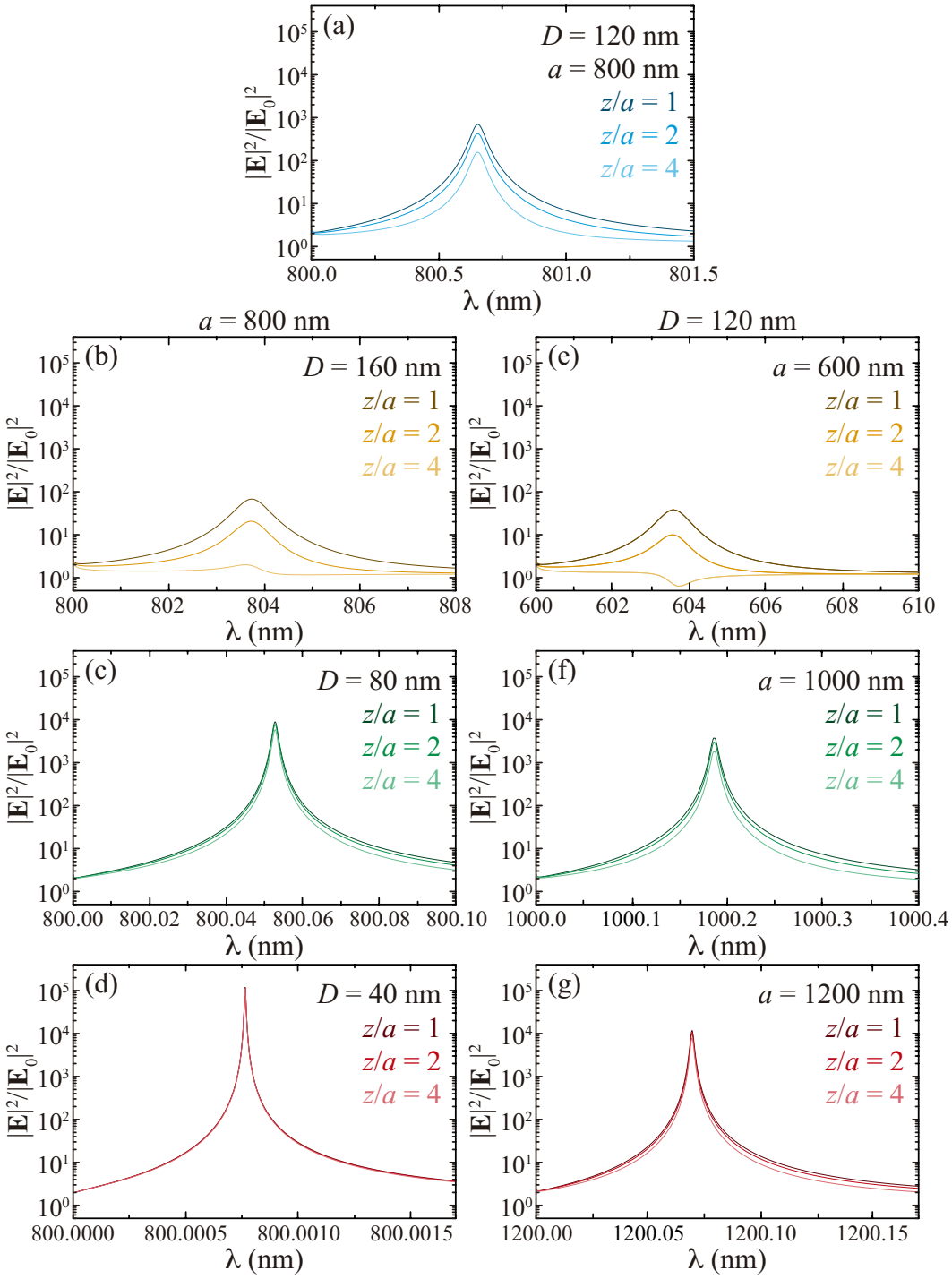

Figure S3: Plot of the near-field intensity enhancement of all cases from Figure 2(a) and (c) of the main paper, but as a function of λ rather than Δ. (a) Plot for $D = 120\,\text{nm}$, $a = 800\,\text{nm}$. (b-d) Plot for a constant periodicity $a = 800\,\text{nm}$ and diameters $D = 160\,\text{nm}$ (b), $D = 80\,\text{nm}$ (c), and $D = 40\,\text{nm}$ (d). (e-g) Plots for a constant diameter of $D = 120\,\text{nm}$ and periodicity $a = 600\,\text{nm}$ (e), $a = 1000\,\text{nm}$ (f), and $a = 1200\,\text{nm}$ (g). In all panels, the shade of the curve color indicates the distance from the array, as indicated by the legend.

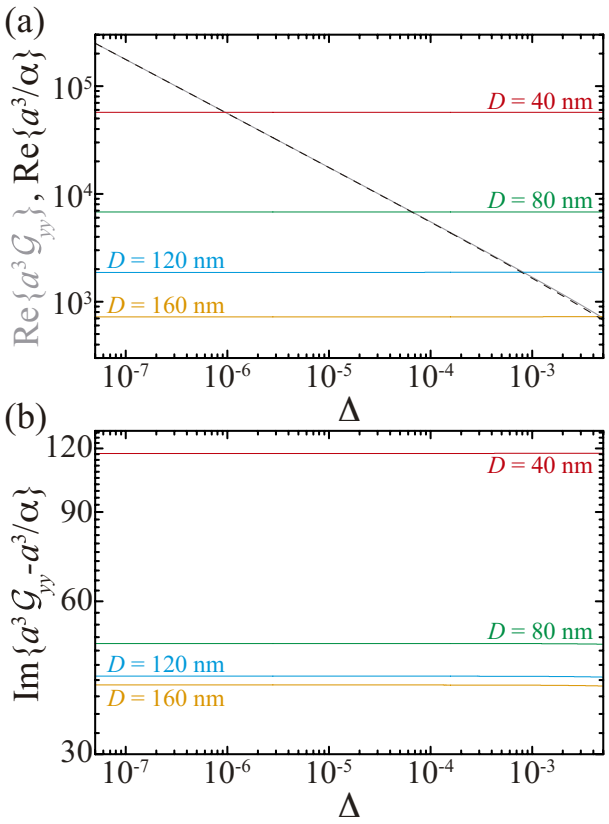

Figure S4: Analysis of the mechanism determining the linewidth of the lattice resonances. (a) Real part of the inverse of the polarizability for particles with different diameters (color curves) compared with the real part of the in-plane component of the lattice sum (gray curve). The black dashed curve represents the approximate value of $\mathrm{Re}\{a^3\mathcal{G}_{yy}(0)\} \approx 4\sqrt{2}\pi^2\Delta^{-1/2} - 118$.[S1,S2] (b) Imaginary part of the difference between the in-plane component of the lattice sum and the inverse of the particle polarizability for the same nanoparticles as in panel (a). In all cases, we assume $a = 800\,\mathrm{nm}$.

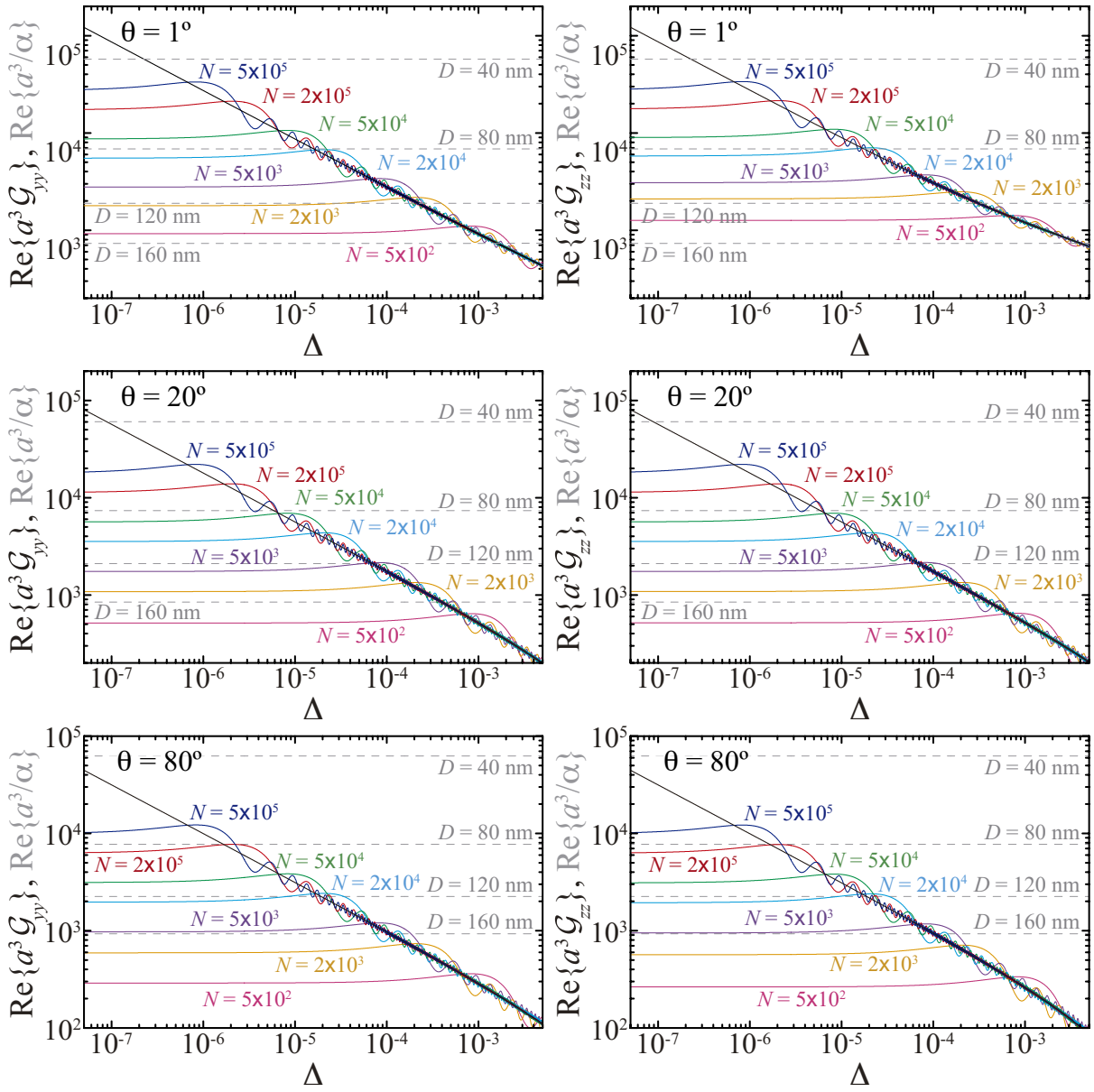

Figure S5: Finite-size effects on the lattice sum. Real part of the in-plane (*i.e.*, yy, left column) and the out-of-plane (*i.e.*, zz, right column) of the lattice sum calculated for different angles of incidence (black curve). The color curves represent the results obtained by truncating the lattice sum for an array of size $(N+1)\times(N+1)$, as described in the main paper (see Figure 5). The gray dashed lines indicate the real part of the inverse of the nanoparticle polarizability calculated for different values of D. In all cases, we assume $a = 800\,\text{nm}$.

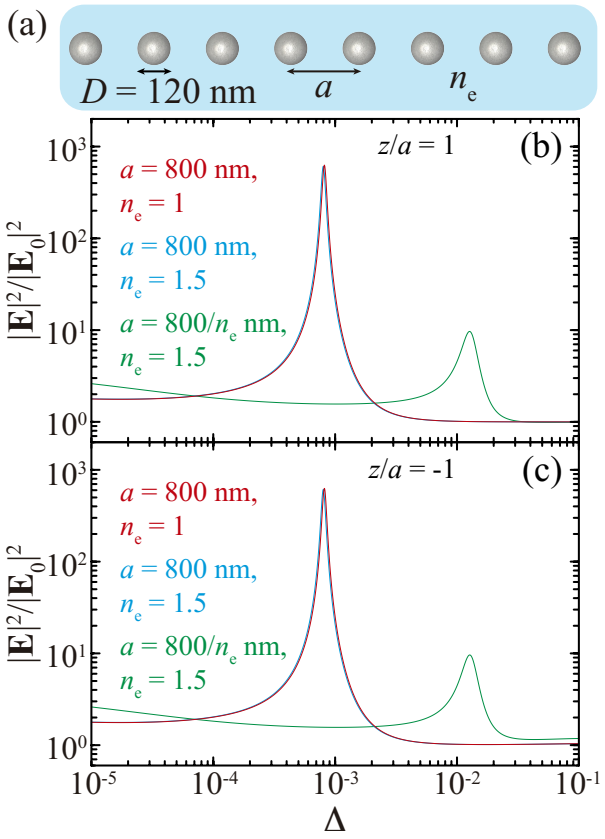

Figure S6: Analysis of the effect of a homogeneous dielectric environment. (a) Schematics of the system under consideration, consisting of an array of silver nanospheres of diameter $D = 120\,\text{nm}$ and periodicity a embedded in a medium of refractive index n_e. (b,c) Near-field intensity enhancement as a function of $\Delta = \lambda/(an_\text{e}) - 1$ for an array of periodicity $a = 800\,\text{nm}$ in vacuum (red curve) and in a medium with $n_\text{e} = 1.5$ (blue curve), as well as for an array with periodicity $a = 800/n_\text{e}\,\text{nm}$ in a refractive index $n_\text{e} = 1.5$ (green curve). In panel (b), the field intensity enhancement is calculated at a height $z = a$ above the array, while, in panel (c), the calculation is done at $z = -a$. Examining these results, we observe that the near-field intensity enhancement produced by the two arrays with $a = 800\,\text{nm}$ are identical, and therefore the only effect of the change in the dielectric environment is a shift of the wavelength of the resonance (notice that now Δ depends on n_e). Such shift can be compensated by decreasing the array periodicity to $a = 800/n_\text{e}\,\text{nm}$, however that results in an increase of the value of Δ of the lattice resonance and, therefore, in a reduction of the field enhancement produced by the array.

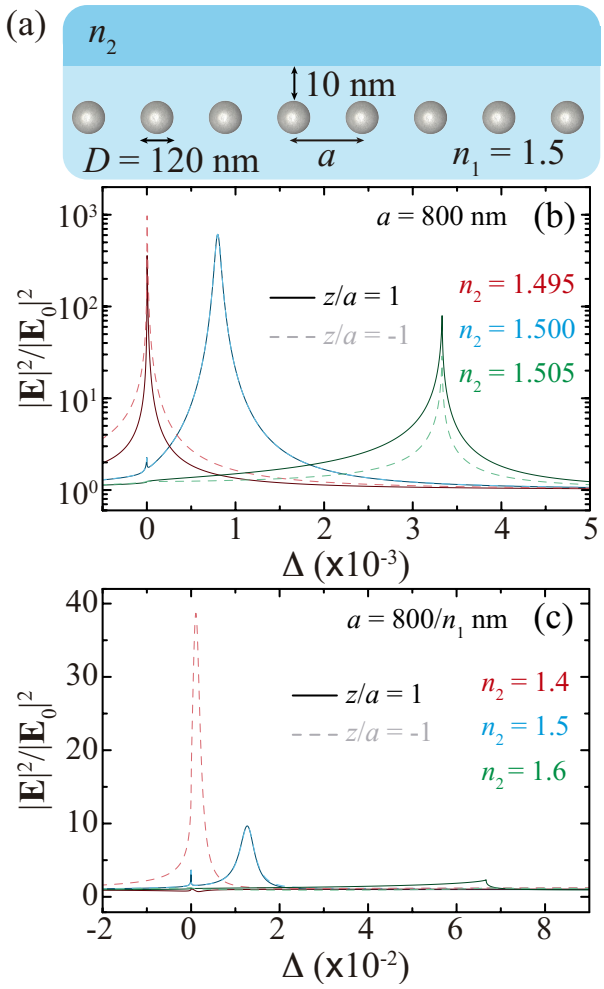

Figure S7: Analysis of the effect of an inhomogeneous dielectric environment. (a) Schematics of the system under consideration, consisting of an array of silver nanospheres of diameter $D = 120\,\text{nm}$ and periodicity a embedded in a medium of refractive index $n_1 = 1.5$ and situated a distance 10 nm from another medium with refractive index n_2. As in the main paper, we assume light is incident from below the array (*i.e.*, from the side with n_1), which is located at $z = 0$. (b) Near-field intensity enhancement as a function of $\Delta = \lambda/(an_1) - 1$ for an array of periodicity $a = 800\,\text{nm}$ when $n_2 = 1.495$ (red curves), $n_2 = 1.5$ (blue curves), and $n_2 = 1.505$ (green curves). The dark solid curves correspond to the case in which the field is calculated at a distance $z/a = 1$ from the array, while the dashed lighter curves display the results for $z/a = -1$. (c) Same as (b), but for an array with periodicity $a = 800/n_1\,\text{nm}$. In this case, the red, blue, and green curves correspond to $n_2 = 1.4$, $n_2 = 1.5$, and $n_2 = 1.6$, respectively. Examining the results of panel (b), we observe that, due to the large field enhancement, the system is very sensitive to asymmetries in the dielectric environment. When $n_2 < n_1$, the lattice resonance shifts to smaller Δ, which leads to an increase in the near-field enhancement, while, for $n_2 > n_1$, the resonance moves to larger values of Δ, thus leading to a decrease in the enhancement. On the other hand, systems producing smaller field enhancements, such as the array analyzed in panel (c), are less sensitive to asymmetric environments.

References

(S1) García de Abajo, F. J.; Gómez-Medina, R.; Sáenz, J. J. Full Transmission Through Perfect-Conductor Subwavelength Hole Arrays. *Phys. Rev. E* **2005**, *72*, 016608.

(S2) García de Abajo, F. J. Colloquium: Light Scattering by Particle and Hole Arrays. *Rev. Mod. Phys.* **2007**, *79*, 1267–1290.